Coastal observations of weather features in Senegal during the African Monsoon Multidisciplinary Analysis Special Observing Period 3

G. Jenkins, P. Kucera, E. Joseph, J. Fuentes, A. Gaye, J. Gerlach, F. Roux, Nicolas Viltard, Mathieu Papazzoni, Alain Protat, et al.

▶ **To cite this version:**

G. Jenkins, P. Kucera, E. Joseph, J. Fuentes, A. Gaye, et al.. Coastal observations of weather features in Senegal during the African Monsoon Multidisciplinary Analysis Special Observing Period 3. Journal of Geophysical Research: Atmospheres, 2010, 115 (D18), pp.D18108. 10.1029/2009JD013022 . hal-00476466

HAL Id: hal-00476466
https://hal.science/hal-00476466

Submitted on 4 Mar 2016

HAL is a multi-disciplinary open access archive for the deposit and dissemination of scientific research documents, whether they are published or not. The documents may come from teaching and research institutions in France or abroad, or from public or private research centers.

L'archive ouverte pluridisciplinaire **HAL**, est destinée au dépôt et à la diffusion de documents scientifiques de niveau recherche, publiés ou non, émanant des établissements d'enseignement et de recherche français ou étrangers, des laboratoires publics ou privés.

Coastal observations of weather features in Senegal during the African Monsoon Multidisciplinary Analysis Special Observing Period 3

G. Jenkins,[1] P. Kucera,[2] E. Joseph,[1] J. Fuentes,[3] A. Gaye,[4] J. Gerlach,[5] F. Roux,[9] N. Viltard,[6] M. Papazzoni,[6] A. Protat,[6,7] D. Bouniol,[8] A. Reynolds,[10] J. Arnault,[9] D. Badiane,[4] F. Kebe,[4] M. Camara,[11] S. Sall,[4] S. A. Ndiaye,[4] and A. Deme[4]

Received 15 August 2009; revised 8 February 2010; accepted 23 April 2010; published 18 September 2010.

[1] During 15 August through 30 September 2006 (Special Observing Period 3, SOP3), key weather measurements are obtained from ground and aircraft platforms during the African Monsoon Multidisciplinary Analysis campaign. Key measurements are aimed at investigating African easterly waves (AEWs) and mesoscale convective systems in a coastal environment as they transition to the eastern Atlantic Ocean. Ground and aircraft instruments include polarimetric radar, a coarse and a high-density rain gauge network, surface chemical measurements, 12 m meteorological measurement, broadband IR, solar and microwave measurements, rawinsonde, aircraft dropsonde, lidar, and cloud radar measurements. Ground observations during SOP3 show that Senegal was influenced by 5 squall lines, 6 Saharan air layer intrusions, and 10 AEWs. Downstream tropical cyclones developed were associated with the passage of four AEWs. FA-20 aircraft measurements of microphysical aspects of 22 September squall line and several nondeveloping AEWs over the extreme eastern Atlantic Ocean are presented.

Citation: Jenkins, G., et al. (2010), Coastal observations of weather features in Senegal during the African Monsoon Multidisciplinary Analysis Special Observing Period 3, *J. Geophys. Res.*, *115*, D18108, doi:10.1029/2009JD013022.

1. Introduction

[2] During NH summer season (JJAS), West African precipitation events occur at mesoscales but may be forced by weather systems occurring on multiple spatial and temporal scales. At the largest-scale African easterly waves (AEWs), which occur on 3–5 day time scales and at wavelengths of 2500–3000 km [*Burpee*, 1975] producing mesoscale precipitation near or ahead of its trough axis. Mesoscale convective systems (MCSs) (squall lines, mesoscale convective complexes, nonsquall tropical clusters) can be initiated and organized by the African easterly jet (AEJ) along with locally generated convection is often found to have a diurnal cycle with many MCSs occurring between 1800 and 0600 LST [*Mathon and Laurent*, 2001].

[3] MCSs are known to contribute to a large fraction of the total rain in West Africa [*D'Amato and Lebel*, 1998]. Long-lived squall lines (SLs) can move rapidly westward traversing large areas of West Africa providing much needed rainfall for agriculture [*Fortune*, 1980; *Gaye et al.*, 1995]. Results from two field experiments (GATE and COPT-81) during the 1970s and 1980 provide much of our understanding about MCSs, especially SLs [*Houze*, 1977; *Chong et al.*, 1987; *Roux et al.*, 1984; *Roux*, 1988], while more recent studies have focused on satellite-derived properties of MCSs in West Africa [*Laing et al.*, 1999; *Nesbitt et al.*, 2000; *Sealy et al.*, 2003]. An SL passage is typically associated with rising surface pressure, reductions in temperature and dew point, and changes in wind speed and direction [*Chong et al.*, 1987].

[4] Once AEWs move from continental to oceanic conditions, approximately 10% develop into tropical systems (tropical depression, storms, or hurricanes). Past studies have linked Atlantic hurricanes to wet conditions in West Africa, but the set of processes responsible for tropical cyclogenesis in the tropical eastern Atlantic remains unclear [*Gray and Landsea*, 1992; *Landsea and Gray*, 1992]. Limited aircraft and ground-based studies have examined

[1]Department of Physics and Astronomy, Howard University, Washington, District of Columbia, USA.
[2]National Center for Atmospheric Research, Boulder, Colorado, USA.
[3]Department of Meteorology, The Pennsylvania State University, University Park, Pennsylvania, USA.
[4]Laboratory for Atmospheric-Oceanic Simeon Fongang (LPAO-SF), Cheikh Anta Diop University, Dakar, Senegal.
[5]NASA Wallops Flight Facility, Wallops, Virginia, USA.
[6]LATMOS (Laboratoire Atmosphères, Milieux, Observations Spatiales), Vélizy, France.
[7]CAWCR (Centre for Australian Weather and Climate Research), Melbourne, Australia.
[8]GAME/CNRM, CNRS/Météo-France, Toulouse, France.
[9]Laboratoire d'Aérologie, Observatoire Midi-Pyrénée, Toulouse, France.
[10]NASA Goddard Space Flight Center, Greenbelt, Maryland, USA.
[11]Department of Physics, University of Ziguinchor, Ziguinchor, Senegal.

Copyright 2010 by the American Geophysical Union.
0148-0227/10/2009JD013022

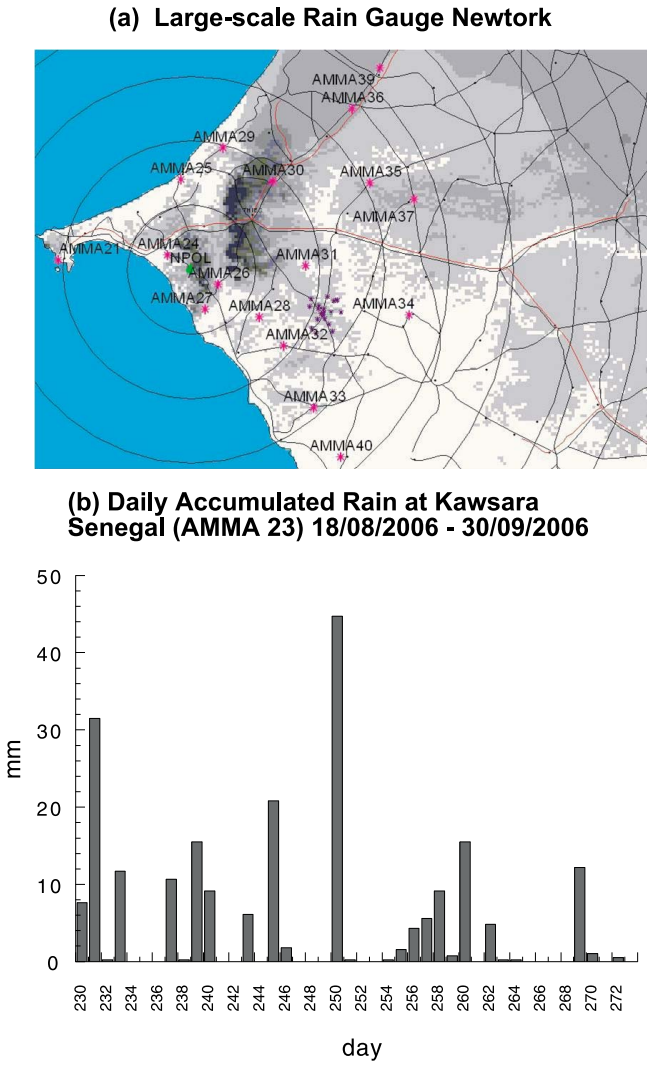

Figure 1. (a) Rain gauge network and (b) 18 August to 30 September daily rain accumulation at Kawsara (AMMA23 gauge).

developing tropical cyclones off the coast of Senegal [*Zipser and Gautier*, 1978; *Sall and Sauvageot*, 2005].

[5] During the summer of 2006, in concert with the African Monsoon Multidisciplinary Analysis (AMMA) campaign [*Redelsperger et al.*, 2006], there was an opportunity to examine tropical cyclogenesis and MCSs in a coastal or marine environment during the Special Observing Period 3 (SOP3; 15 August to 30 September 2006). SOP3 is the peak of the West African monsoon period followed by a retreat during late September. Moreover, Atlantic tropical cyclone activity is increasing, with the peak in hurricane frequency occurring on approximately 10 September. Aircraft (DC-8) and ground measurements were deployed in Cape Verde for the period of 15 August to 15 September during NASA African Monsoon Multidisciplinary Analysis, denoted as NAMMA [*Zipser et al.*, 2009], and in Senegal for the period of 15 August to 30 September. Ground measurements (18 August to 15 September) are highlighted in the first half of section 3, and aircraft measurements (16–30 September) are highlighted in the second half of section 3.

[6] The coastal location of Senegal provides a unique setting for ground base and aircraft measurements to examine (1) the properties of MCS, as they transition from continental to maritime environmental conditions; (2) the dynamic/thermodynamic aspects of westward propagating AEWs, which could potentially developing into tropical cyclones over the eastern Atlantic; and (3) Saharan air layer (SAL) intrusions and associated environmental changes. Senegal is centered between 12°N–17°N and 11°W–18°W and is bound to the north by arid conditions and to the south by humid conditions. Senegal borders the eastern Atlantic Ocean, and there are elevated regions in the southeast part of the country (Fouta Djallon).

2. Ground and Aircraft Measurements

2.1. Ground Measurements

[7] During the SOP3 period, ground-based measurements were primarily obtained at Kawsara (14.66°N, 17.10°W) Senegal. During the period of 15 August to 30 September, two radiosoundings per day were launched from the airport at Dakar (14.73°N, 17.5°W) during the period of 15–30 September 2006. Kawsara served as the primary site for ground observations between 19 August and 30 September 2006. Table 1 indicates measurements used during SOP3 including a coarse and high-density rain gauge network (Figures 1a and 1b) established within the NPOL radar range throughout the SOP3. From 15 August to 20 September 2006, the UK ATD Lightning Detection Network, based on very low frequency (VLF) arrival time difference (ATD) principles that measures cloud-to-ground (CG) lightning flashes, was employed for continental and oceanic lightning measurements [*Keogh et al.*, 2007].

[8] Six hour National Centers for Environmental Prediction (NCEP) Reanalysis are used for identifying AEWs and space-borne observations from the Tropical Rainfall Measurement Mission (TRMM) overpasses are examined for four squall lines (19 August, 31 August to 1 September, and 11 September) during SOP3 [*Kalnay et al.*, 1996]. Radiosoundings were not available from Dakar Senegal on 23 and 26 August and replaced by radiosounding data from Kawsara. Moreover, there is no radiosounding data on 26 September. Ancillary AMMA data from the aerosol optical thickness (AOT) measurements from the aerosol robotic network (AERONET) at Mbour, Senegal (14.39°N, 16.59°W) are used for the SOP3.

2.2. Aircraft Measurements

[9] There were several flights by the NASA DC-8 near or over Senegal (15 August to 12 September), but most DC-8 missions were over the tropical eastern Atlantic [*Zipser et al.*, 2009]. The FA20 dedicated a number of flights (16–30 September) over Senegal and the extreme eastern Atlantic to examine the modification of the microphysical properties of convective systems as they transition from inland to open ocean. The FA20 with its cloud radar, backscatter lidar, in situ cloud microphysics instruments in combination with the ground-based NPOL polarimetric Doppler radar provide a unique opportunity of examining aerosol, microphysics, cloud properties, and precipitation. Table 2 provides a description of aircraft measurements during the SOP3.

Table 1. Senegal SOP3 Ground Measurements

Instrument	Measured Parameters	Location	Period
Radiosonde (RS-92)	Vertical temperature, wind, and humidity profiles	Dakar, Senegal Kawsara, Senegal	15 August to 30 September, 23 August to 16 September
NASA Polarimetric Radar (NPOL) S Band	Radar reflectivity, Doppler velocity, polarimetric properties, and rainfall estimates	Kawsara, Senegal	21 August to 30 September
Rain gauge network, disdrometer	Rainfall rates, rainfall accumulation, DSD	Western Senegal	15 August to 30 September
Flux tower	Relative humidity, air temperature (1.5, 6, 8, 11 m), sea level pressure, wind speed (12 m), and direction	Kawsara, Senegal	23 August to 16 September

[10] Thirteen FA20 flights were conducted with three main scientific objectives: (1) sample the mesoscale dynamics with dropsondes in order to initialize a mesoscale model; (2) characterize the microphysical and radiative properties of stratiform and cirriform parts of convective systems inland and over the ocean, as well as the modulation of the convective activity by SAL intrusions with the RALI observations; and (3) produce collocated data sets between RALI and CloudSat/CALIPSO satellite measurements in order to assess the calibration of these spaceborne sensors, only a few months after its launch.

[11] Seven flights were conducted to address the microphysics and CloudSat/CALIPSO validation objectives (18, 20, 21, 22, 26 morning, 26 afternoon, and 27 September), and one flight was dedicated to the characterization of the SAL by the RALI/LNG lidar (29 September). Four of these flights included a flight segment below the A-Train satellite constellation (Aqua, CloudSat, Calipso, Parasol, Aura) [*Stephens et al.*, 2002] swath, four flights were performed over the ocean and three over land or at the transition between land and ocean. One flight was dedicated to an accurate calibration of the RALI/RASTA cloud radar instrument (28 September). Highlights obtained with this data set are given in section 3.

[12] Furthermore, four AEWs (denoted as perturbations A, B, C, and D) were observed with dropsondes released from the SAFIRE (**S**ervice des **A**vions **F**rançais **I**nstrumentés pour la **R**echerche en **E**nvironnement)/FA20 aircraft on 16, 18–19, 23, and 25, 26, 27 September 2006, respectively. Dropsonde data related to perturbation D have been analyzed in the work of *Arnault and Roux* [2010], so we only focus here on the first three observed perturbations.

[13] Eight to twelve dropsondes were launched during each of the four flights of SOP3 Phase III in order to document the mesoscale characteristics of perturbations A, B, and C. The dropsonde sampling covered horizontal domains of approximately 500 km × 500 km with a distance of about 150 km between each sonde. More precisely, 8 successful dropsondes were launched during Flight 67 on 16 September, 10 were launched during Flight 68 on 18 September, 12 were launched during Flight 69 on 19 September, and 9 were launched during Flight 73 between on 23 September.

[14] The dropsonde data allowed for derivation of three-dimensional fields of wind components, temperature, and humidity using the technique developed by *Moine* [2001]. Vertical cross sections of these composite fields are discussed in parallel with ECMWF (European Centre for Medium-Range Weather Forecast) analyzed heights and winds at pressure levels 300, 700, and 1000 hPa, and Meteosat-9 images in the water vapor channel at 7.3 μm in order to document the synoptic and convective environment of perturbations A, B, and C. Together, the ground and aircraft measurements during SOP3 provide a unique data set of MCSs/AEWs properties in a coastal environment of the Sahel.

3. Results

[15] In this section, we summarize important features for the three 15 day periods: Phase 1 (15–31 August), Phase 2 (1–15 September), and Phase 3 (16–30 September). Phases 1–2 focus on ground measurements, while Phase 3 is focused on FA20 aircraft measurements. Figure 1b shows the accumulated daily rain for the rain gauge located near the NPOL radar at Kawsara. The heaviest rain event occurred on Julian day 250 (7 September) with the passage of an AEW. Moderate precipitation fell on Julian day 231 (19 August) with the passage of a squall line, which produced a significant area of stratiform rain that fell for several hours.

3.1. SOP3 Phase 1 (15–31 August)

3.1.1. AEW and SAL Intrusions

[16] Figures 2a–2f shows NCEP reanalysis and radiosondes data for Dakar Senegal for 15–31 August 2006. The

Table 2. Senegal SOP3 FA-20 Aircraft Measurements

Instrument	Measured Parameters	Location	Period
RALI instrument (RASTA cloud radar and LNG lidar)	Radar reflectivity and Doppler velocity, lidar backscatter, cloud microphysical and radiative properties	FA-20 (Dakar)	16–30 September
In situ microphysical probes	In situ cloud microphysics	FA-20 (Dakar)	16–30 September
Dropsondes	Vertical profiles of temperature, wind, relative humidity	FA-20 (Dakar)	16–30 September

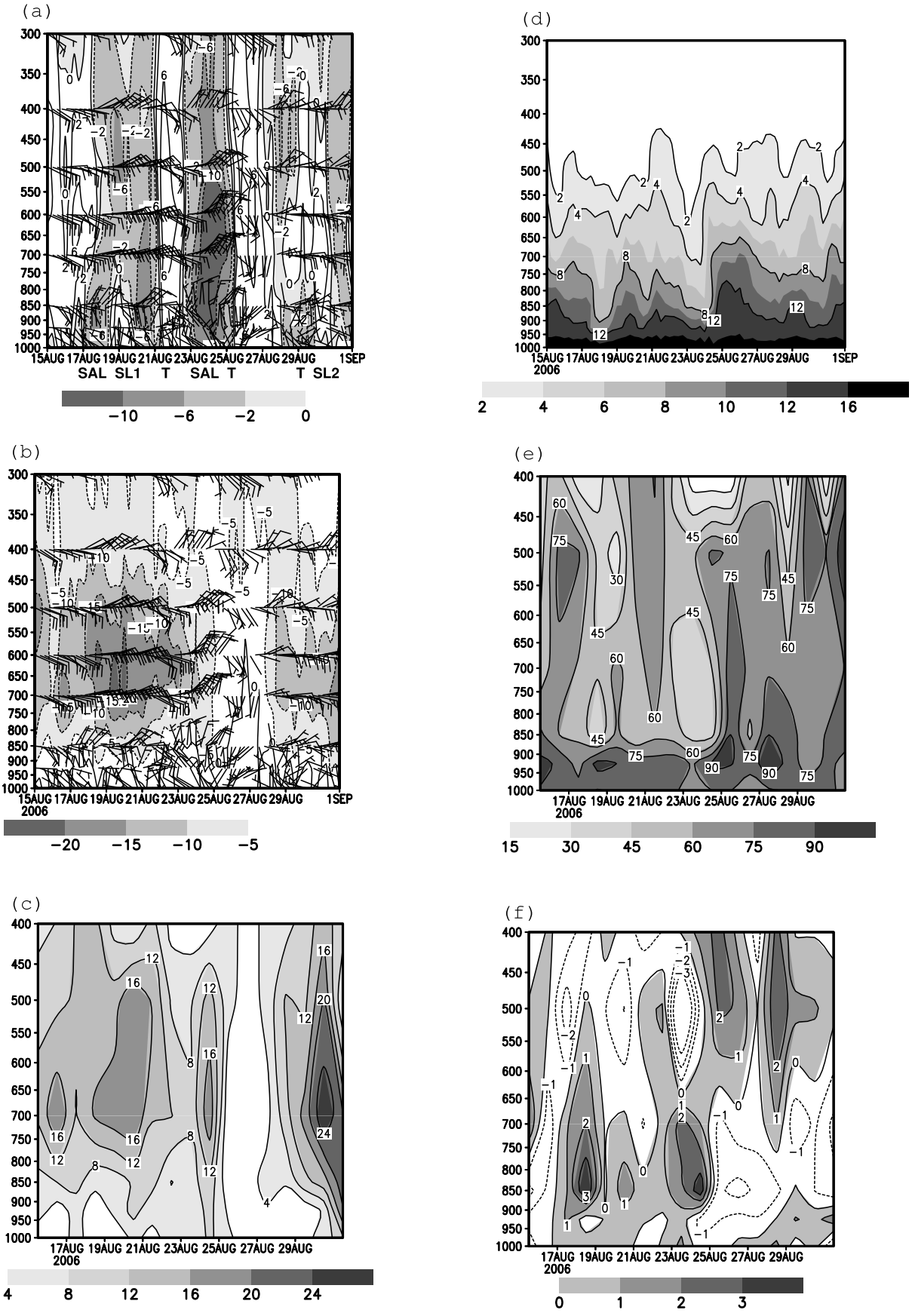
(a)
SAL SL1 T SAL T T SL2
−10 −6 −2 0
(b)
−20 −15 −10 −5
(c)
4 8 12 16 20 24
(d)
2 4 6 8 10 12 16
(e)
15 30 45 60 75 90
(f)
0 1 2 3
15AUG 17AUG 19AUG 21AUG 23AUG 25AUG 27AUG 29AUG 1SEP
2006

Figure 2

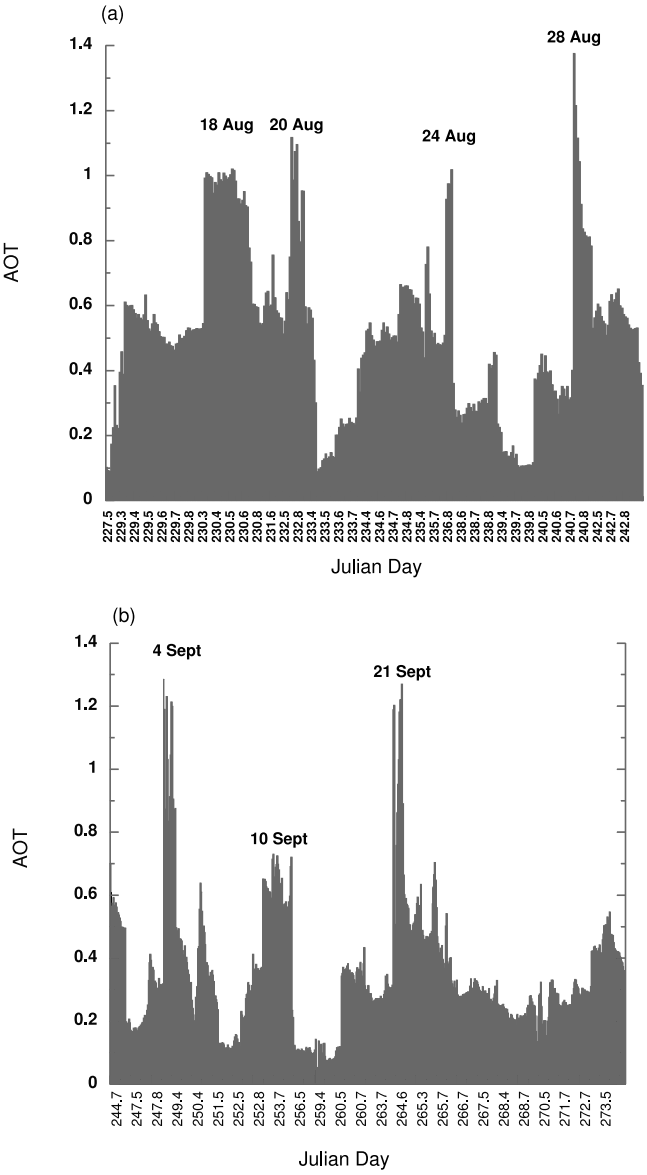

Figure 3. AOT at 440 μm at Mbour Senegal for (a) 15–31 August and (b) 1–30 September.

NCEP meridional winds (Figure 1a) show three AEWs passing Dakar during this 15 day period with the trough axis (denoted T). The AEW passage on 21 August was associated with the formation of tropical depression (later TS Debby) whose northern rainband crossed Dakar, Senegal [*Jenkins et al.*, 2008] on morning of 20 August. Strong winds between 700 and 500 hPa are found at Dakar from the reanalysis and observed data at Dakar for this event (Figures 2b and 2c). Strong zonal winds are also found on 24 and 30–31 August from the Dakar sounding. The NCEP reanalysis specific humidity shows several dry intrusions (Figure 2d), which are associated with northerly winds on 18, 21, and 24 August (Figure 2a). The radiosounding data from Dakar also confirms these as low relative humidity days (Figure 2e), which are colocated with warm temperature perturbations located at 850 hPa (Figure 2f). Aerosol optical thickness (AOT) measurements from Mbour, Senegal, also show peaks on 18, 20, and 24 August (Figure 3). Although high AOT values are found on 28 August, there is no evidence of a SAL event based on a relatively moist sounding at Dakar. The high AOT values were associated with clouds as precipitation was found on 28 August at Kawsara and identified from visible satellite images.

3.1.2. Observed Squall Lines

[17] There were two squall lines on 19 and 31 August (denoted as SL1 and SL2) that moved into Senegal. Ground-based NPOL observations from Kawsara were not available for SL1, but TRMM overpasses were available along with synoptic and upper air observations from Dakar. SL1 had its origins in Western Niger on the morning of 18 August, moved westward into Mali, and entered Senegal by 1200 UTC 19 August (Figures 4a and 4b). METEOSAT-derived cloud top temperatures warmed as the system entered into Senegal, suggesting weakening but later cooled with increased lightning concentrated as SL1 approached the coastline (Figures 4c and 4d). A SAL outbreak, which occurred on 18 August, was still evident from the 1200 UTC 19 August and 0000 UTC 20 August sounding at Dakar (not shown), suggesting that increased lightning and colder cloud tops could indicate convective cloud invigoration through dust/cloud microphysics interactions near the coastline [*Jenkins et al.*, 2008].

[18] A TRMM precipitation radar (PR) overpass of this squall line as it entered into Senegal at 1147 UTC 19 August shows a north-south band of high reflectivity with the convective core showing >35 dBZ values below 5 km followed by a stratiform rain region (Figures 5a and 5b). Strong northeasterly winds above 800 hPa are found prior to the squall line arriving at Dakar but shift to southwest following SL1 passage from the surface through 500 hPa (Figures 5c and 5d).

[19] SL2 originated in Central Mauritania late on 30 August moved toward the southwest crossing into Senegal at approximately 0400 UTC, 31 August (not shown). SL2 was associated with a fast moving jet streak at 700–600 hPa in southern Mauritania with strong convection observed at 0600 UTC (Figure 6a). SL2 crossed Kawsara at approximately 0800 UTC with areas of lightning concentrated along its path and near the coastline (Figures 6b, 6c, and 6d). Evidence of a low-latitude trough is seen to the southeast of Senegal.

[20] A TRMM overpass of SL2 at 0535 UTC shows a leading band of convection that is oriented from NW to SE and maximum reflectivity values of 40–45 dBZ (Figure 7a). A vertical cross section at 15.1°N shows a leading edge convective tower that reached above 10 km, with an area of trailing stratiform rain (Figure 7b). Vertical profiles of wind

Figure 2. (a) 15–31 August NCEP V, (b) NCEP U, (c) Dakar wind speed, (d) NCEP specific humidity, (e) Dakar relative humidity, and (f) Dakar potential temperature differences. Saharan air layer (SAL), squall line (SL), and trough (T) are identified in Figure 2a. Units: wind, m s^{-1}; specific humidity, g kg^{-1}; temperature, °C.

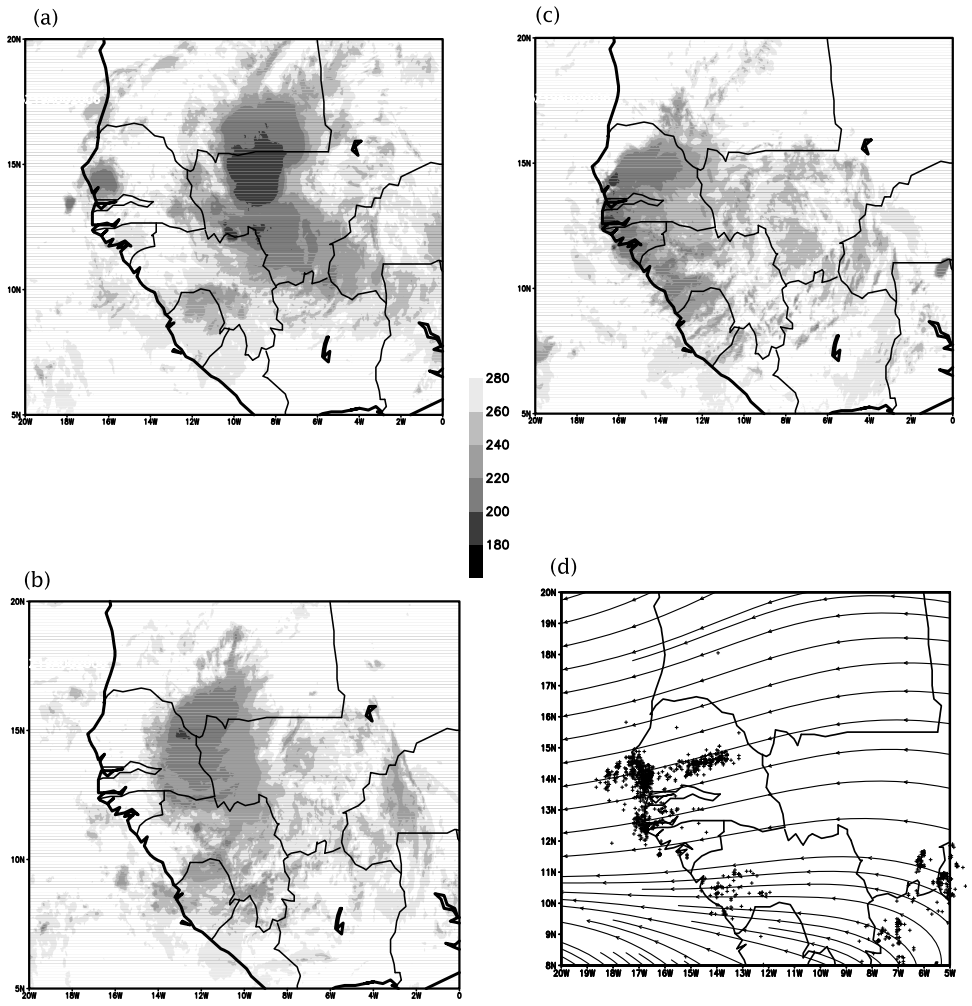

Figure 4. 19 August cloud top temperatures at (a) 0600 UTC, (b) 1200 UTC, (c) 1600 UTC, and (d) NCEP 1200 UTC 700 hPa streamlines overlain with lightning from 1200 to 1800 UTC.

at Kawsara at 0000 and 1152 UTC show an increase in wind speed in the lower (surface to 850 hPa) and midtroposphere (700–500 hPa) and a shift in winds with a southerly component to a northerly component (Figures 7c and 7d).

[21] At 0800 UTC, NPOL radar analysis of SL2 at 4 km altitude also show the leading band of convection in the range of 40–50 dBZ, similar to the TRMM estimates (Figure 8a). The leading convective cell is confined to altitudes somewhat less than the TRMM PR (10 km) and is consistent with warming cloud top temperatures as SL2 moved southwestward. The trailing stratiform rain is found to extend more than 80 km behind the leading line (Figure 8b). Flux tower measurements at Kawsara show significant changes in near surface values at approximately 0800 UTC, consistent with the time of the NPOL estimates. A 1.5 hPa increase in surface pressure, a 3°C reduction in temperature, a 7 m s^{-1} increase in wind speeds, and a sharp shift in wind directions from 320° to 70° is noted with the passage of the squall line (Figures 8c and 8d). A detailed analysis of SL2's lifecycle is provided by *Delonge et al.* [2010], and the role of convective downdrafts in SL2, a surface enhancement of O_3, is provided by *Grant et al.* [2008].

3.2. SOP3 Phase II (1–15 September)

3.2.1. AEW and SAL Intrusions

[22] Figures 9a–9f show NCEP reanalysis and radiosonde derived data from Dakar, Senegal, for 1–15 September 2006. The NCEP meridional wind (Figure 9a) shows three AEWs passing Dakar during this 15 day period. The wave passage on 2 September was associated with the disturbance that later formed into Hurricane Gordon. The wave passage on 11–12 September was associated with the formation of tropical depression 8 (later Hurricane Helene). Strong winds between 700 and 500 hPa are found at Dakar from the reanalysis and observed data at Dakar at the beginning of the month and in the 11–12 September period (Figures 9b and 9c). Strong winds are also found at Dakar from the sounding data on 8 September with the passage of a nondeveloping AEW. The NCEP reanalysis specific humidity shows several periods of dry intrusions (Figure 9d), which are associated with northerly winds on 4–6 and 11 September (Figure 9b). The radiosounding data from Dakar also confirms these as low relative humidity days (Figure 9e) with warm temperature perturbations located near 850 hPa during these time periods (Figure 2f). Elevated aerosol optical

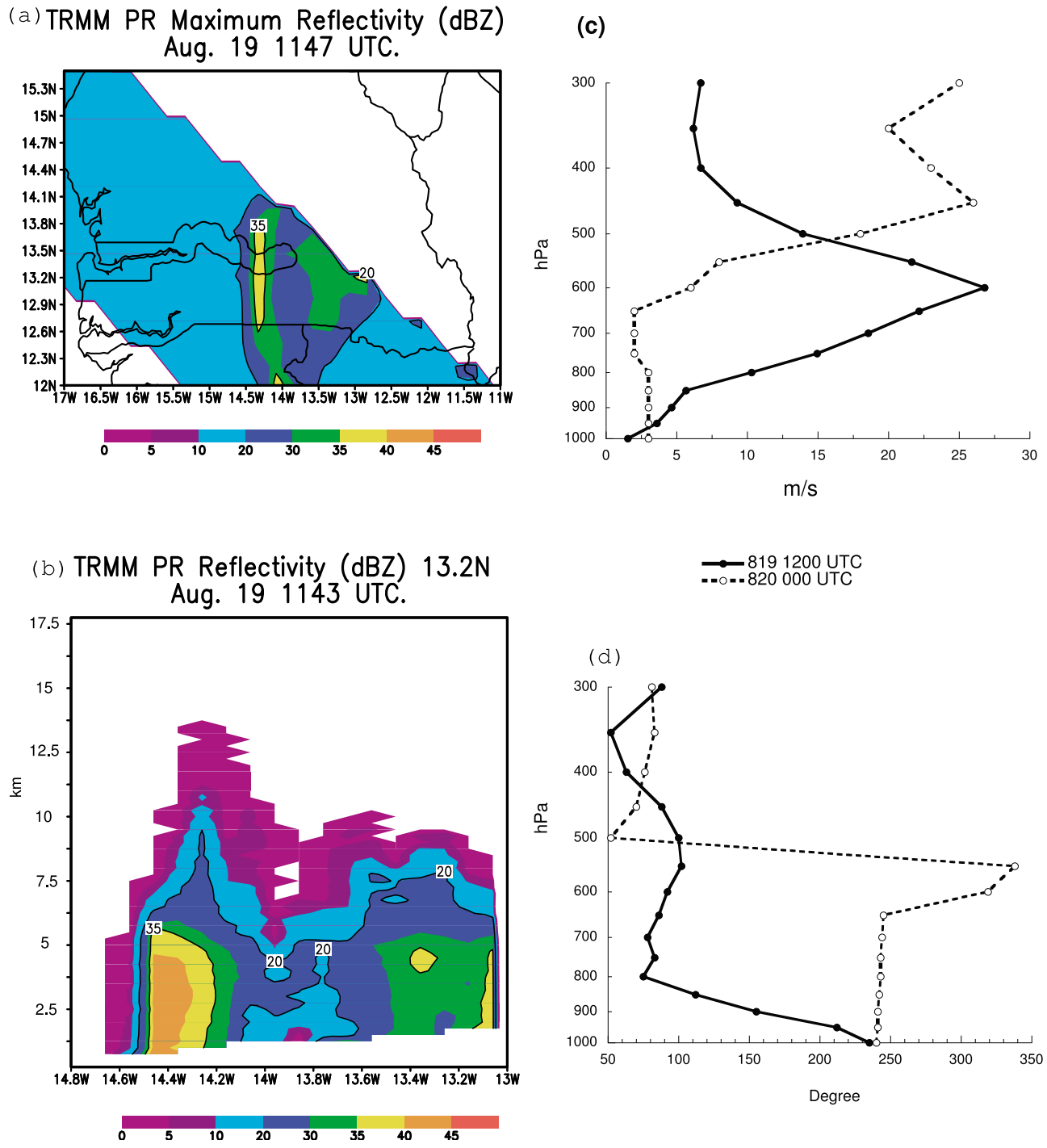

Figure 5. (a) 19 August TRMM maximum reflectivity from 1143 UTC overpass. (b) TRMM cross section of reflectivity at 13.2°N. (c) vertical profiles of wind speed from Dakar on 19 August 1200 UTC and 20 August 0000 UTC. (d) Same as Figure 5c except wind direction.

thickness (AOT) values from Mbour, Senegal, are found on 4 and 10 September (Figure 3b).

3.2.2. Observed Squall Lines

[23] There were two squall lines on 2 and 11 September (denoted as SL3 and SL4) that moved into Senegal and were linked to AEWs. SL3 moved Senegal on 1 September in association with an AEW over Burkina Faso, developed MCC-like features, and moved into Western Mali, where it took on squall line features. At approximately 1800 UTC, the squall line entered Senegal with cloud top temperatures less than 200°K as it approached the coastline (Figures 10a–10c). Numerous lightning strikes are found during the evening of 1 September and early morning hours of 2 September (Figure 10d).

[24] TRMM PR observations at 1858 UTC 1 September show a north-south convective band with maximum re-

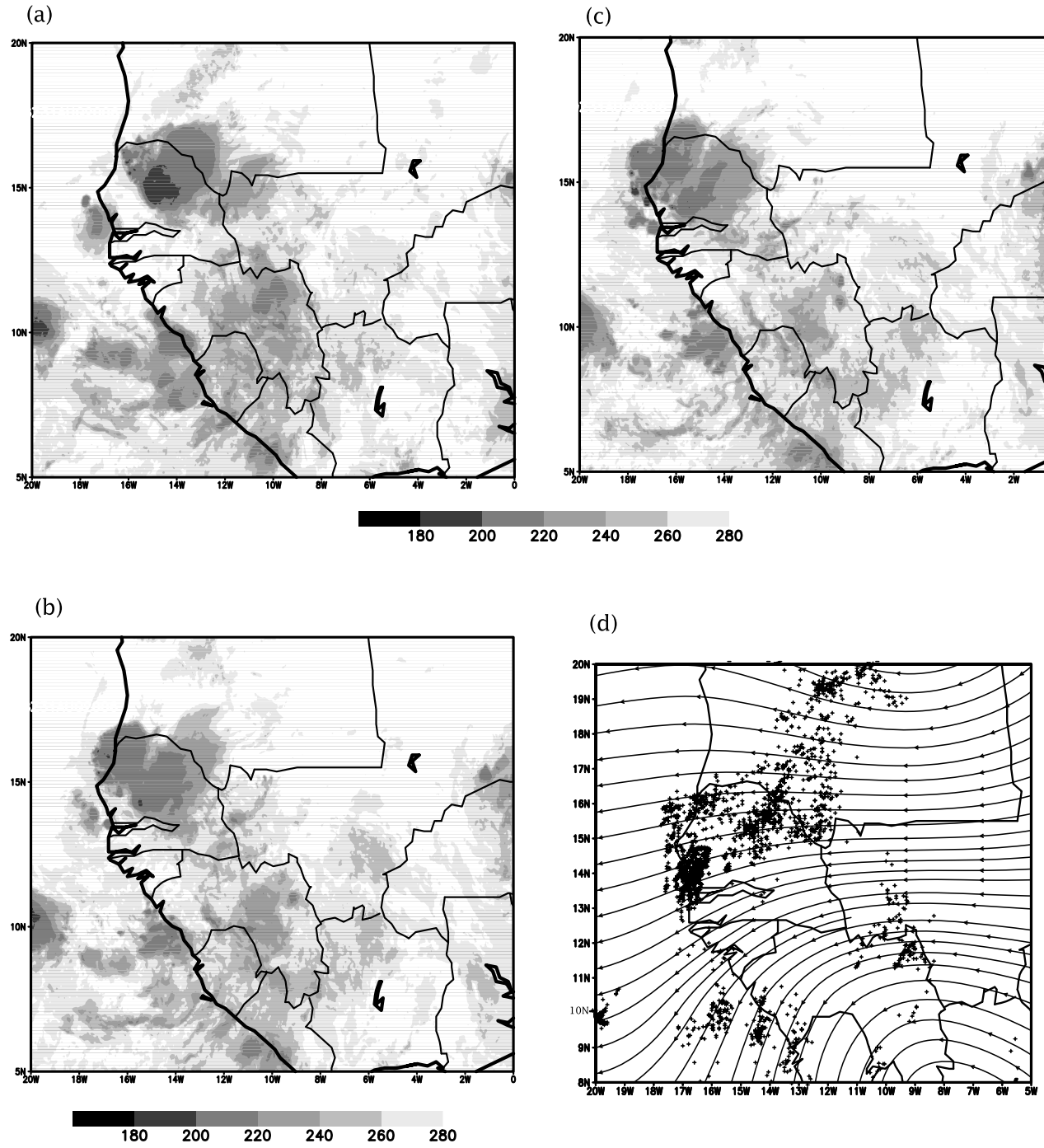

Figure 6. 31 August cloud top temperatures at (a) 0600 UTC, (b) 1200 UTC, (c) 1600 UTC, and (d) NCEP 1200 UTC 700 hPa streamlines overlain with lightning from 1200 to 1800 UTC.

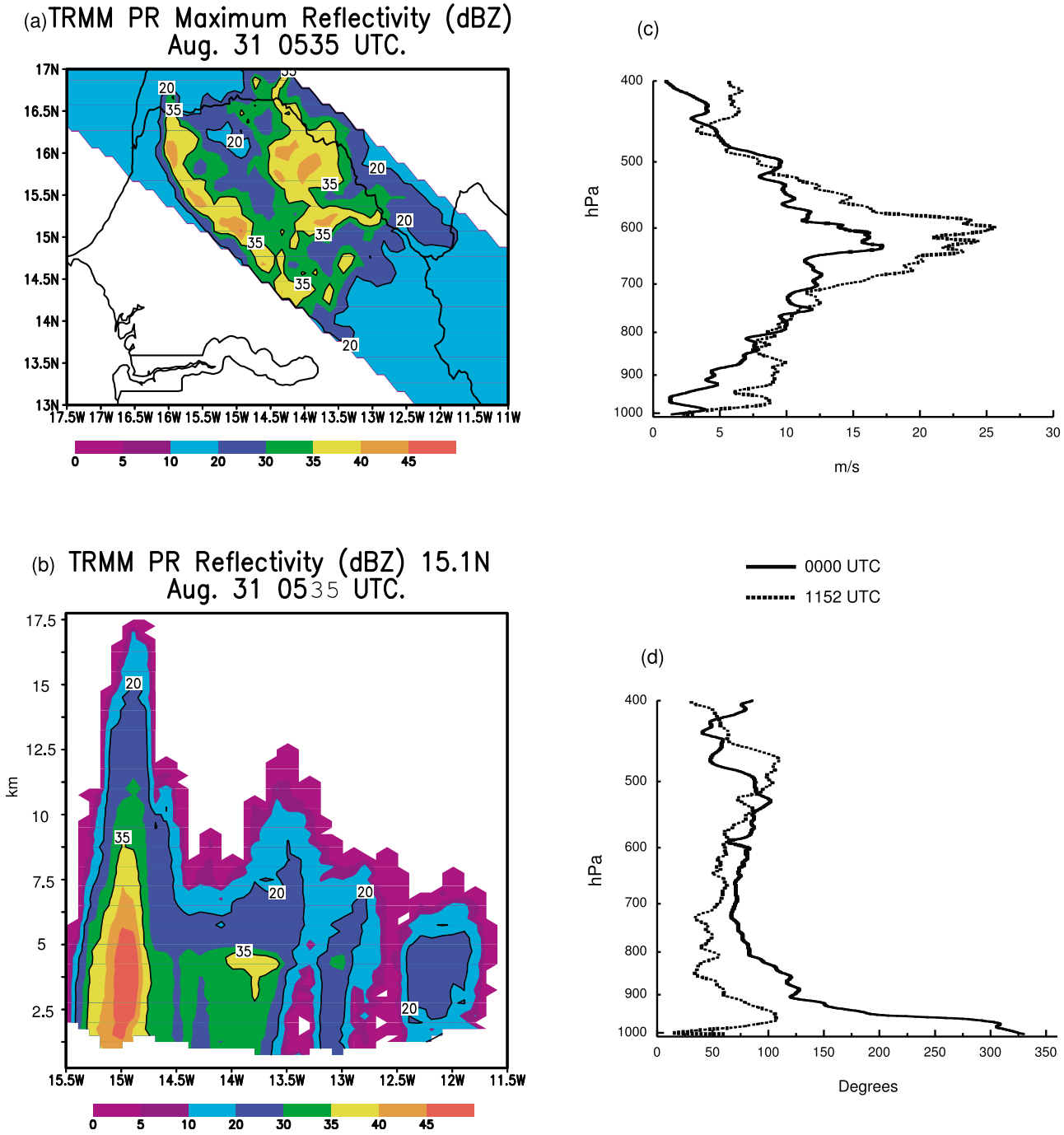

Figure 7. (a) 31 August TRMM maximum reflectivity from 0535 UTC overpass. (b) TRMM cross section of reflectivity at 15.1°N. (c) Vertical profiles of wind speed from Kawsara on 31 August 0000 UTC and 1152 UTC. (d) Same as Figure 7c except wind direction.

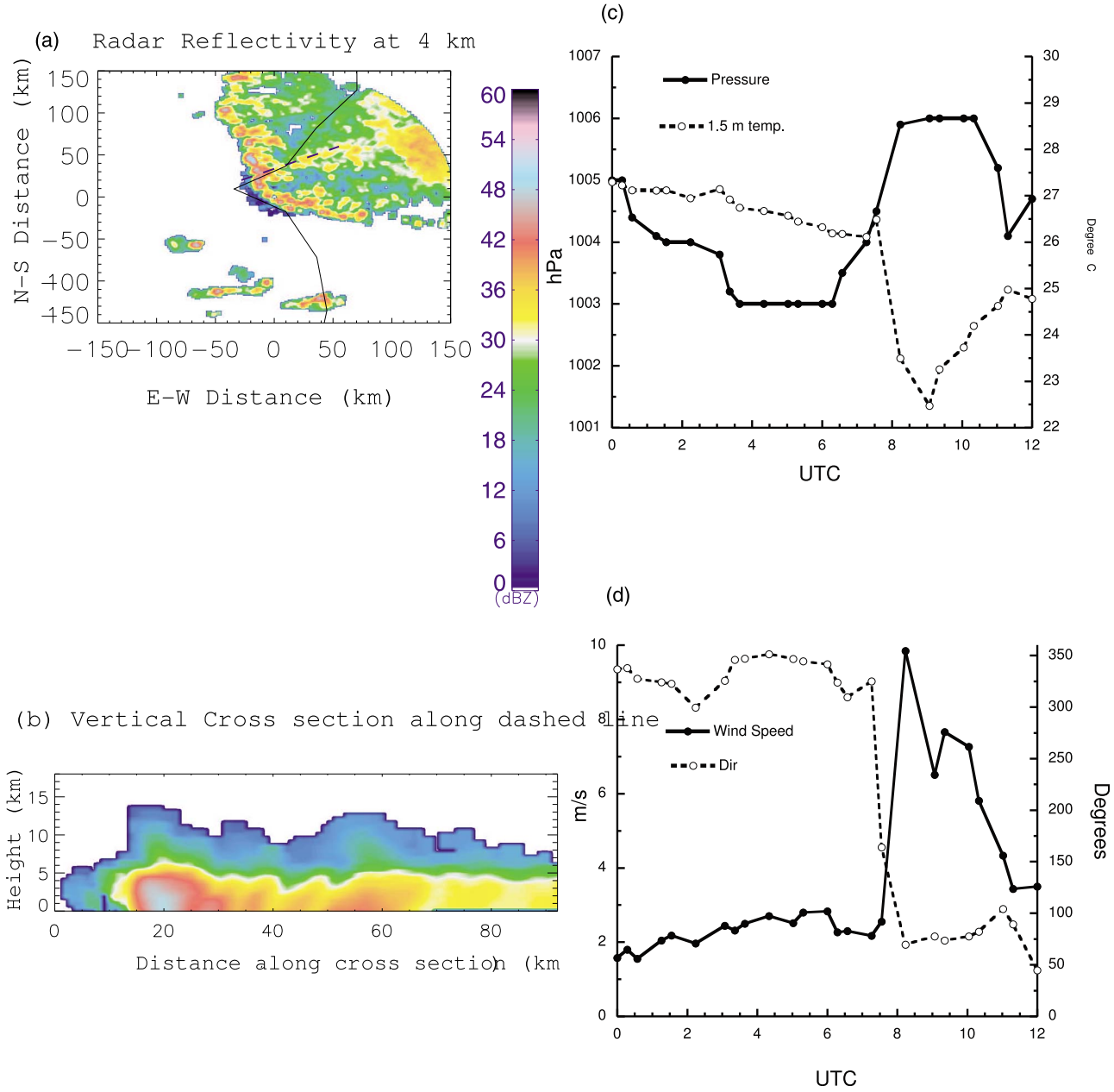

Figure 8. 31 August Kawsara measurements of (a) 0800 UTC NPOL Radar 4 km reflectivity, (b) NPOL cross section of reflectivity (dBz), (c) flux tower 1.5 m pressure and temperature, and (d) 12 m wind speeds and direction.

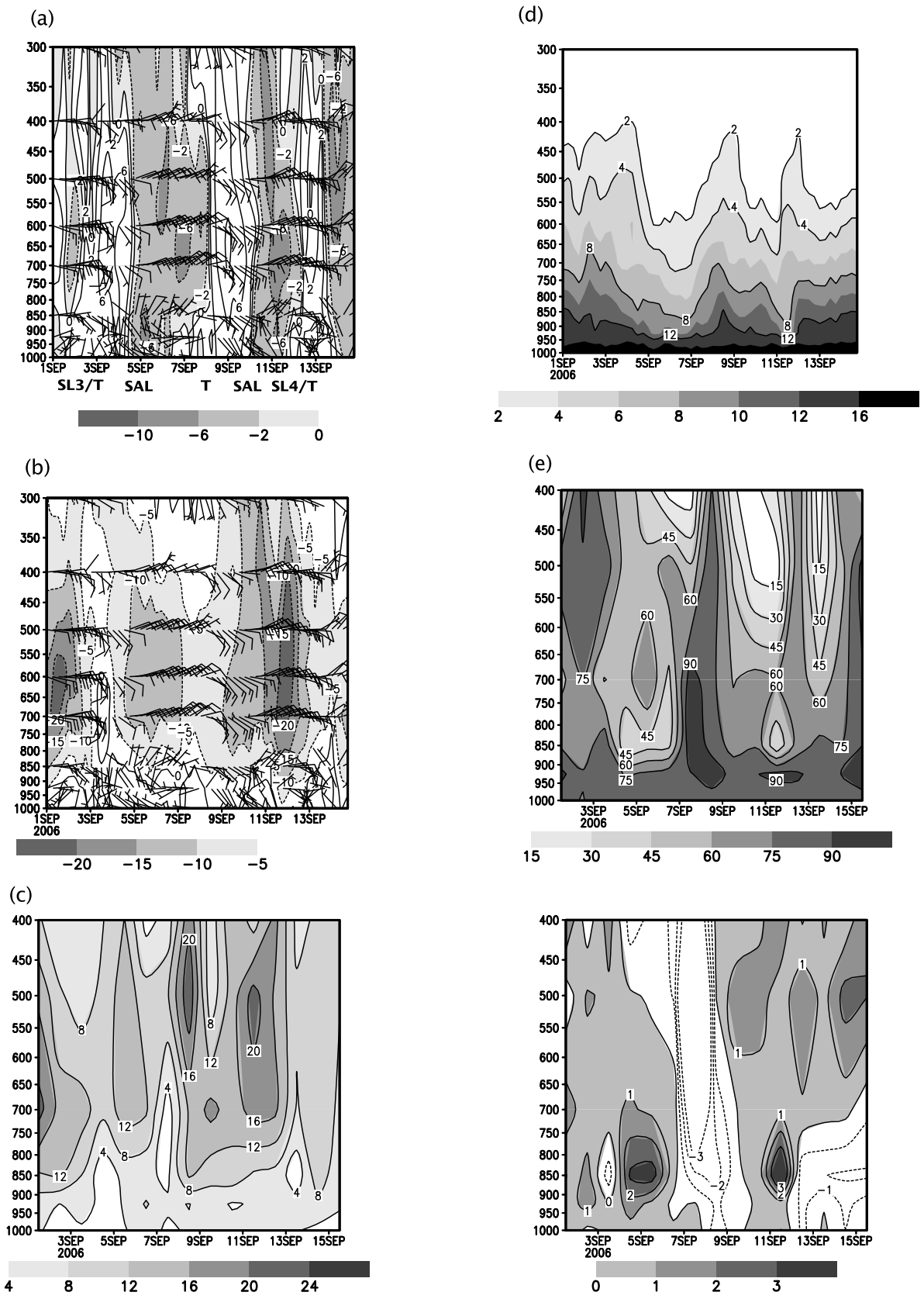

Figure 9. (a) 1–16 September NCEP V, (b) NCEP U, (c) Dakar wind speed, (d) NCEP specific humidity, (e) Dakar relative humidity, and (f) Dakar potential temperature differences. Saharan air layer (SAL), squall line (SL), and trough (T) identified in Figure 9a. Units: wind, m s^{-1}; specific humidity, g kg^{-1}; temperature, °C.

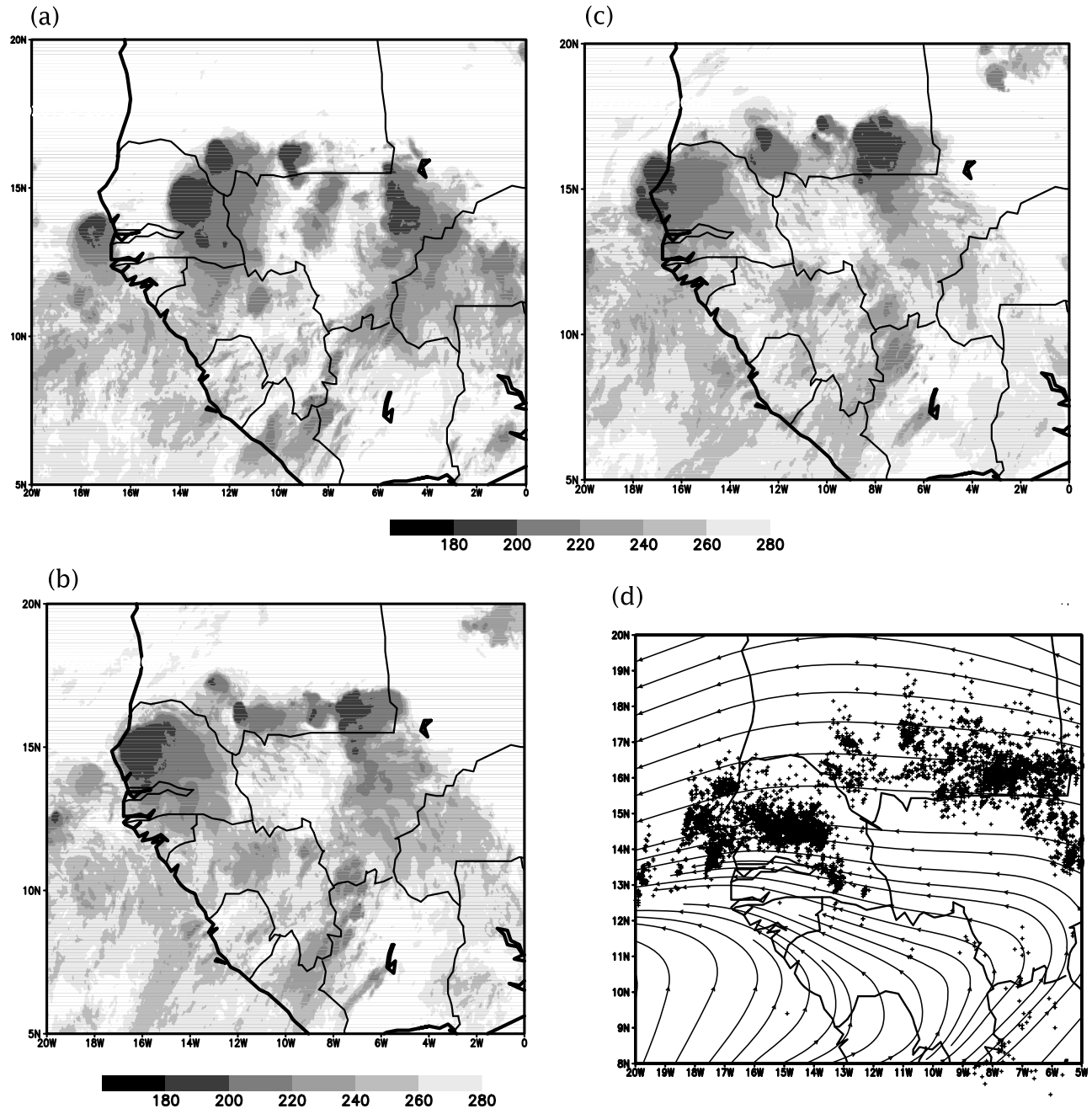

Figure 10. Cloud Top Temperatures at (a) 1 September 2000 UTC, (b) 2 September 0000 UTC, (c) 2 September 0200 UTC, (d) NCEP 0000 UTC 2 September 700 hPa streamlines overlain with lightning from 2000 to 0400 UTC.

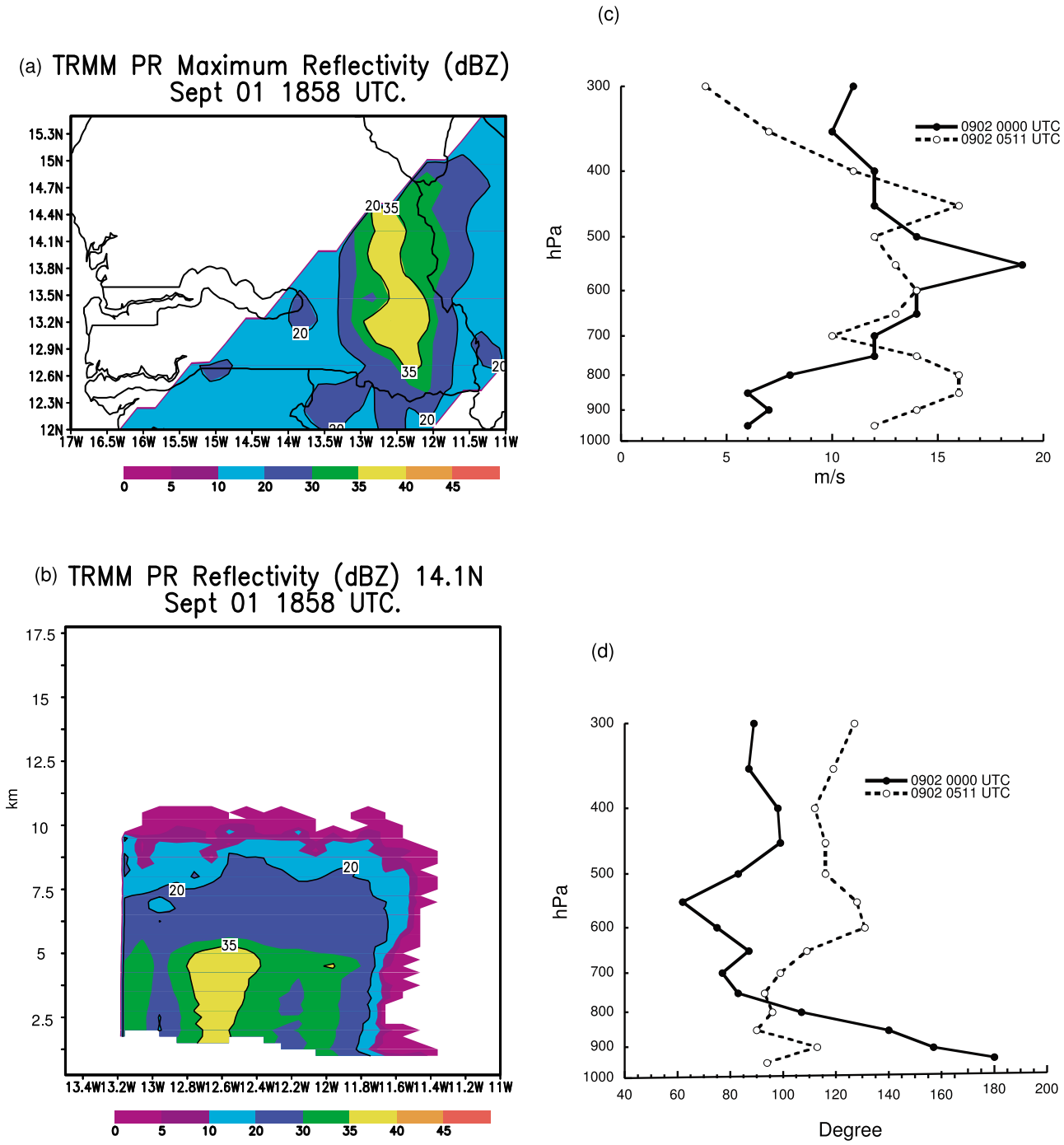

Figure 11. (a) 1 September TRMM maximum reflectivity from 1858 UTC overpass. (b) TRMM cross section of reflectivity at 15.1°N. (c) Vertical profiles of wind speed from Kawsara on 2 September 0000 UTC and 1152 UTC. (d) Same as Figure 11c except wind direction.

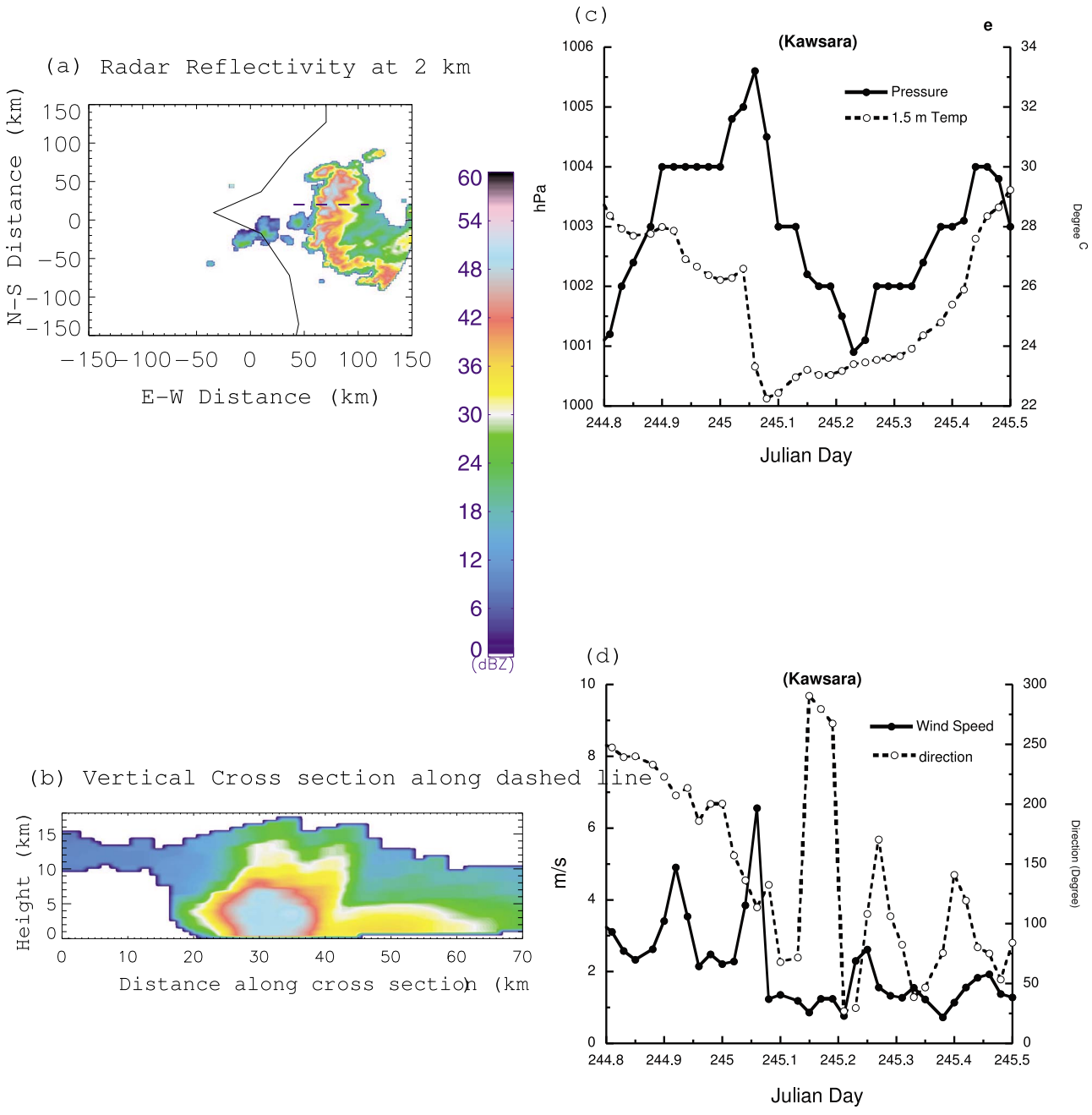

Figure 12. 1–2 September Kawsara measurements of (a) 0000 UTC 2 September NPOL Radar 4 km reflectivity, (b) NPOL cross section of reflectivity (dBz), (c) flux tower 1.5 m pressure and temperature, and (d) 12 m wind speeds and direction.

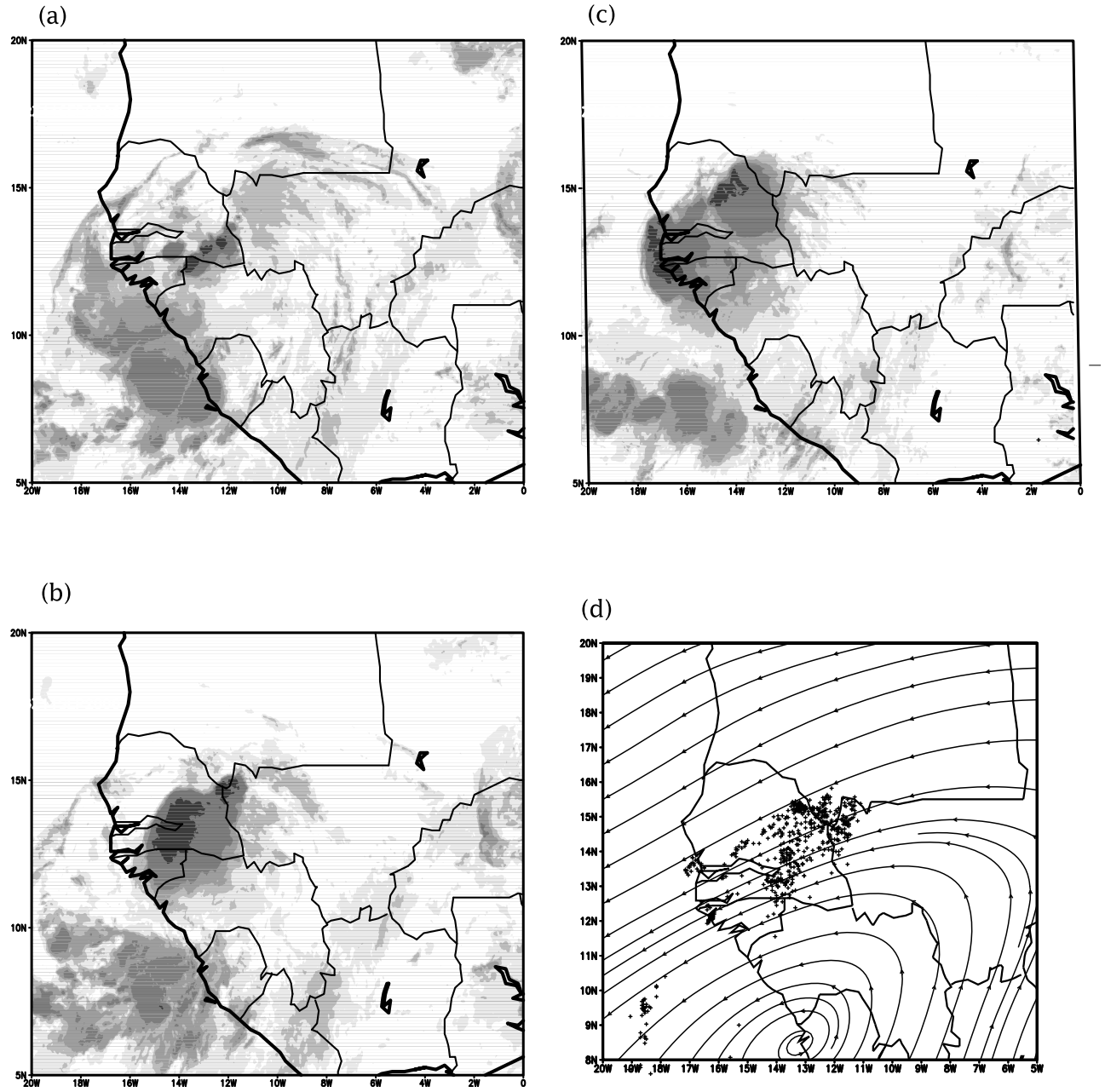

Figure 13. 11 September cloud top temperatures at (a) 0200 UTC, (b) 0600 UTC, (c) 1000 UTC, and (d) NCEP 0600 UTC 700 hPa streamlines overlain with lightning from 0300 to 1000 UTC.

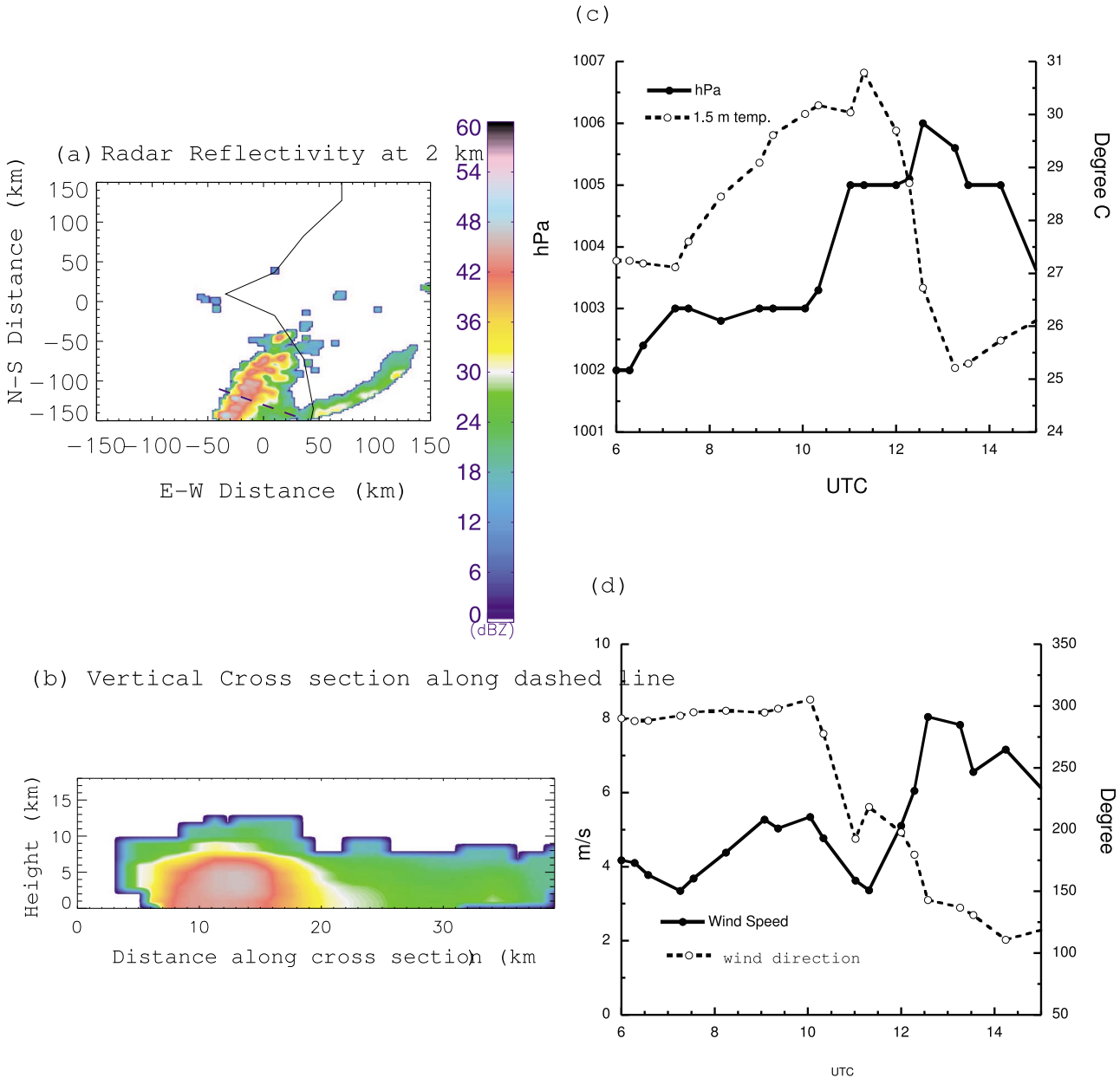

Figure 14. 11 September Kawsara measurements of (a) NPOL Radar 4 km reflectivity, (b) NPOL cross section, (c) flux tower 1.5 m pressure and temperature, and (d) 12 m wind speeds and direction.

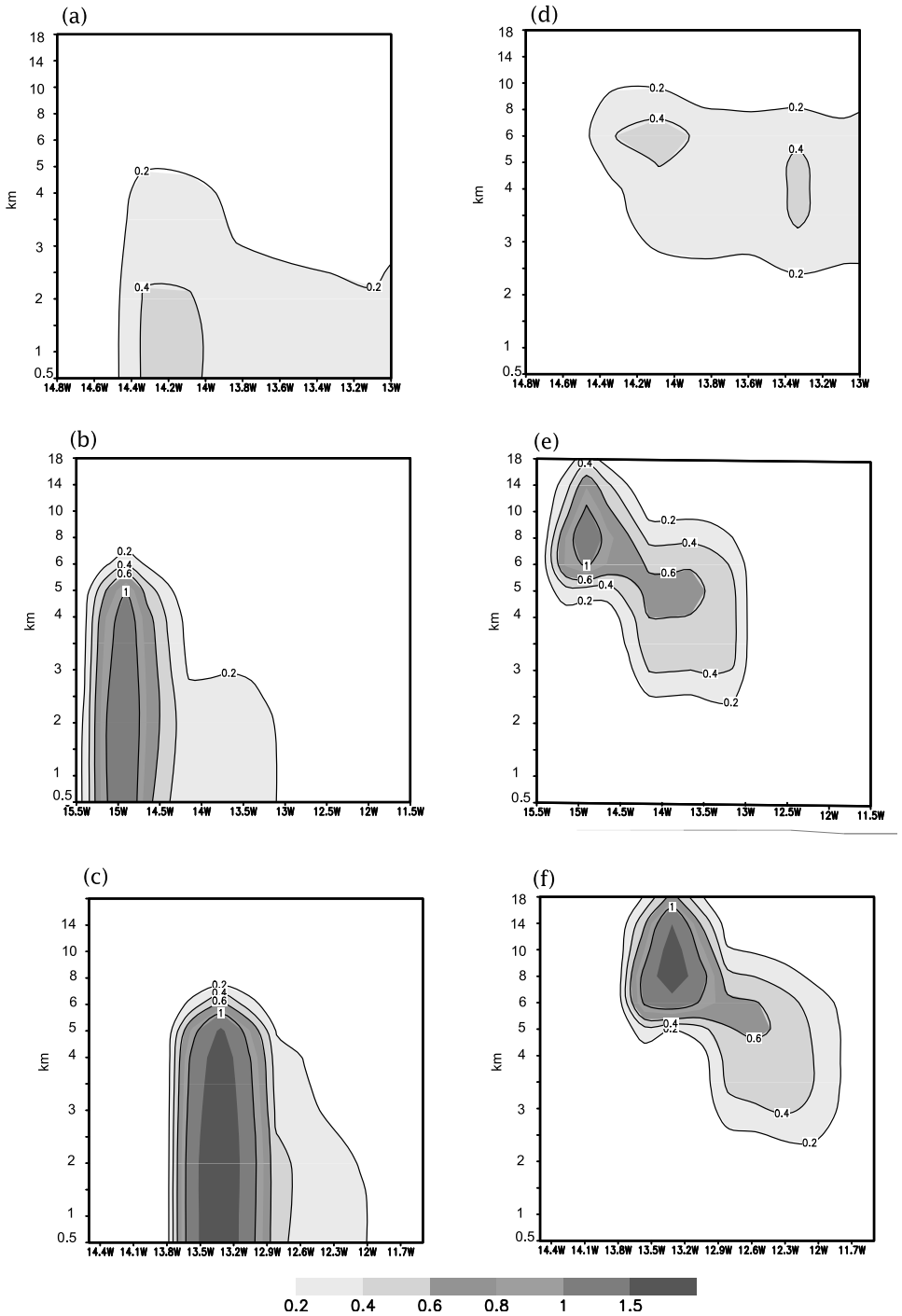

Figure 15. TRMM microphysical properties for (a) 19 August precipitation water, (b) 31 August precipitation water, and (c) 1 September precipitation water and for (a) 19 August precipitation ice, (b) 31 August precipitation ice, and (c) 1 September precipitation ice. Units in g/m^3.

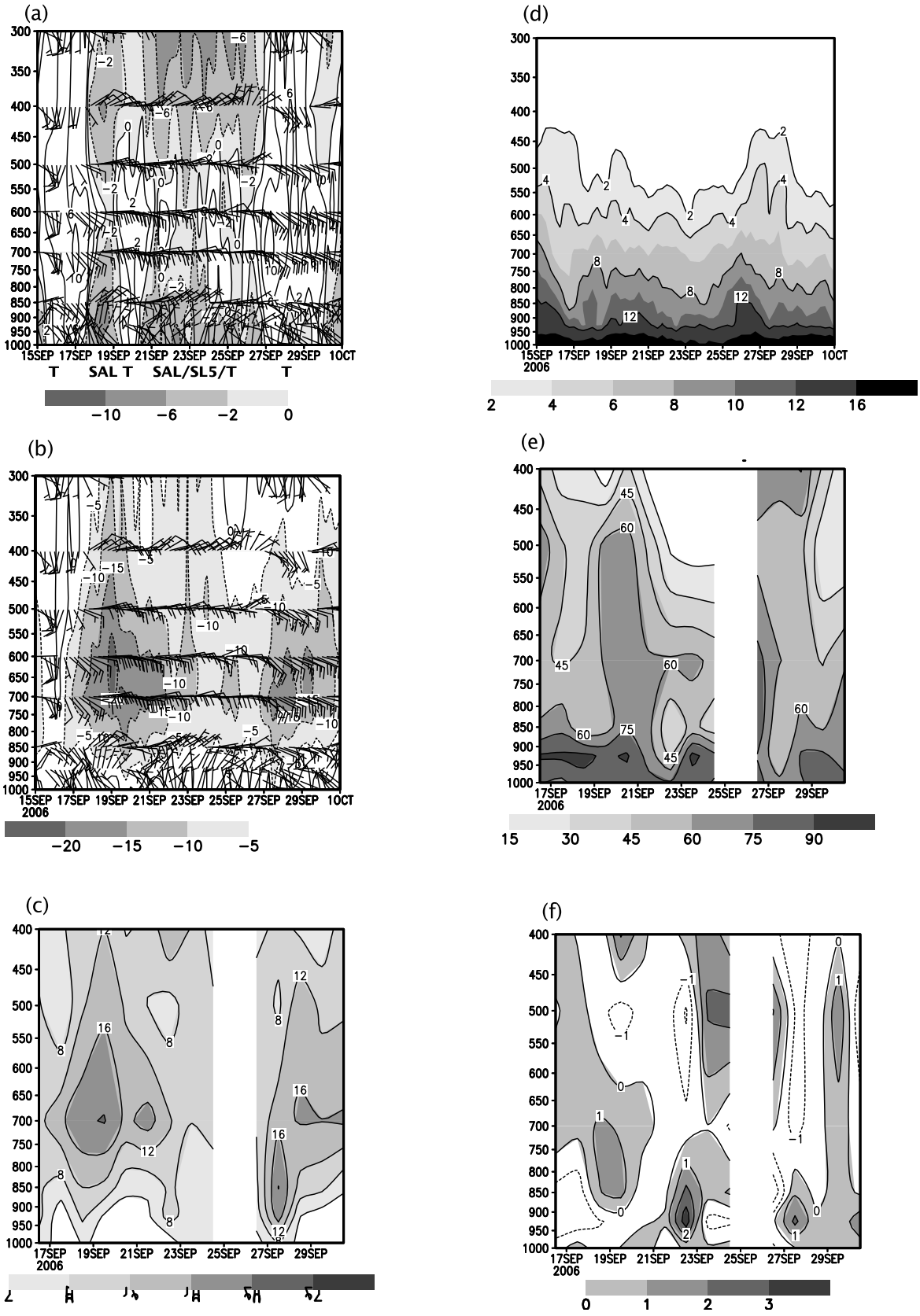

Figure 16. (a) 16–30 September NCEP V, (b) NCEP U, (c) Dakar wind speed, (d) NCEP specific humidity, (e) Dakar relative humidity, and (f) Dakar potential temperature differences. Saharan air layer (SAL), squall line (SL), and trough (T) identified in Figure 16a. Units: wind, m-s^{-1}; specific humidity, g kg^{-1}; temperature, °C.

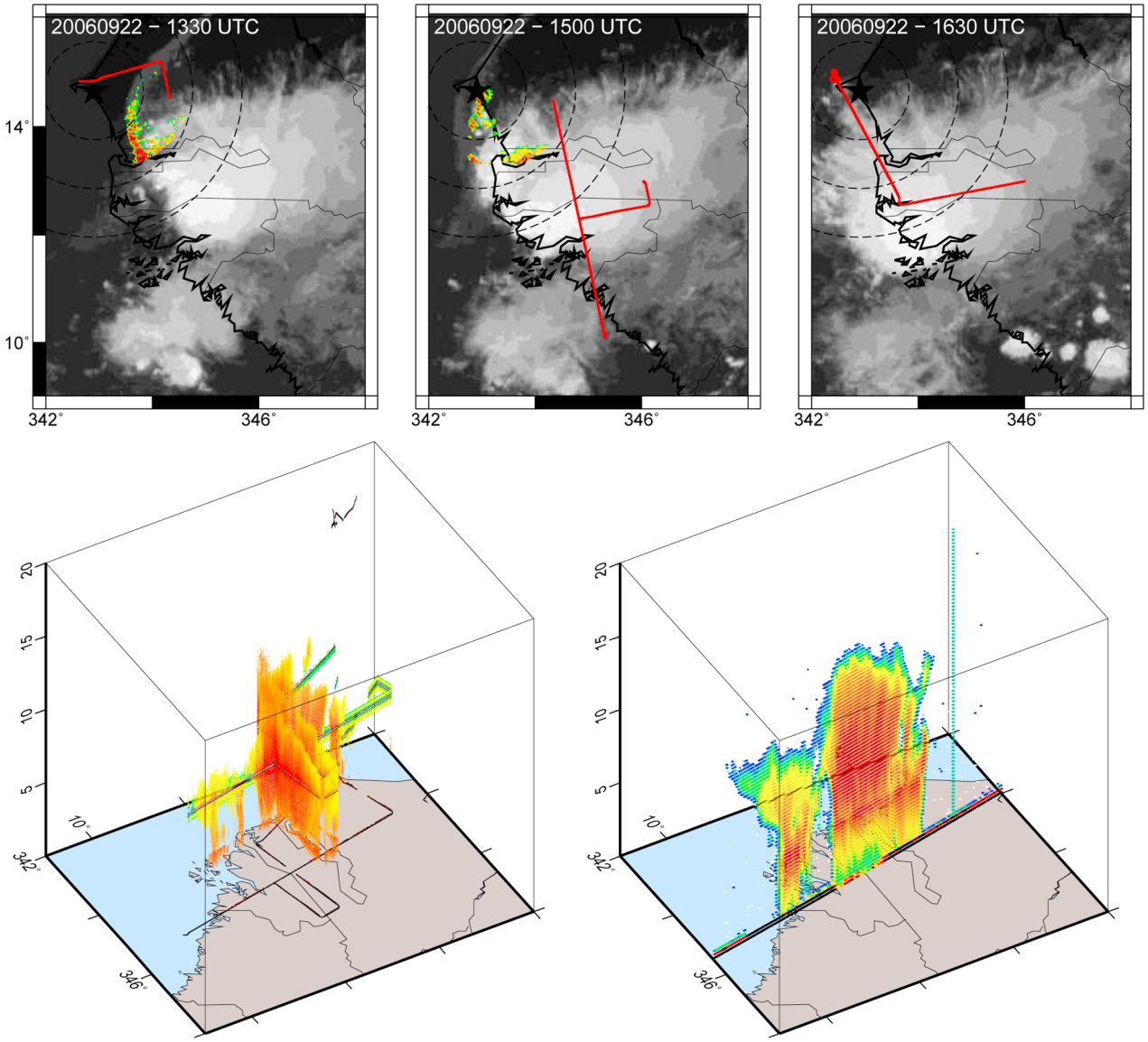

Figure 17. Meteosat brightness temperature in the 10.8 μm channel for the 22 September 2006 at (a) 1330 UTC, (b) 15 UTC, and (c) 1630 UTC with NPOL reflectivity at 2 km height superimposed. Black dashed lines show 100, 200, and 300 km range from Kawsara. (d) RASTA 94 GHz and the corresponding FA20 flight track. (e) CloudSat 94 GHz reflectivity with ground track shown by the black solid lines.

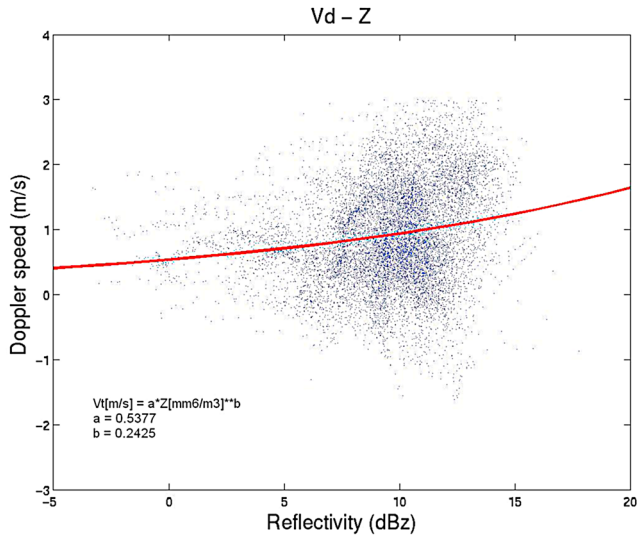

Figure 18. Scatterplot of Nadir Doppler velocity versus radar reflectivity measured by the RASTA 95 GHz Doppler radar for all the Falcon 20 flights during AMMA SOP3. The nonlinear regression to these data points is shown as a red line, and the *a* and *b* parameters are also given.

flectivity values of 35 dBZ (Figure 11a). A convective core near 14.1°N shows the leading convective core confined to 5 km altitude with trailing stratiform rain (Figure 11b). Wind speeds increased below 700 hPa after SL3 passage but were reduced near 500 hPa (Figure 11c). The winds were northeasterly above 800 hPa just prior (0000 UTC 2 September) to SL3 passage with a southerly component afterward (Figure 11d).

[25] The 0000 UTC 2 September NPOL radar data at 4 km altitude show a strong line of convection that is oriented north-south with maximum reflectivity values greater than 45 dBZ (Figure 12a). The vertical cross section shows strong convection extending to altitudes greater than 10 km with an area of trailing stratiform rain (Figure 12b). A 1.5 hPa increase in surface pressure and a 2°C–3°C decrease in temperature occur with the passage of the squall line at approximately 0100 UTC, consistent with conceptual models and observations of MCS passage [*Houze*, 1977]. A 4 m s^{-1} increase in wind speed is noted near the time of passage with a shift to easterly winds after the passage of the squall line (Figures 12c and 12d).

[26] On 11 September, SL4 was generated in response to a strong westward moving AEW that developed into tropical depression 8 on 12 September. SL4 first appeared on at 0200 UTC 11 September and cloud top temperatures continued to cool during the early morning hours (Figures 13a and 13b). By 1000 UTC, the squall line was separated into two parts, with the southern part of SL4 reaching the coastline at approximately 1000 UTC (Figure 13c). Dry air was established over central/northern Senegal throughout the day based on the Dakar/Kawsara soundings, potentially inhibiting development in the northern part of the squall line. Lightning was concentrated in eastern Senegal with the 0600 UTC streamlines showing a vortex near the Guinea border (Figure 13d).

[27] The 1000 UTC NPOL radar data at 4 km altitude examining the southern portion of SL4 shows 35–45 dBZ values with this squall line (Figure 14a). The convective core was confined to altitudes lower than 5 km (Figure 14b). While only a trace of precipitation fell at Kawsara at approximately 1300 UTC, an increase in surface pressure and wind speeds, a decrease surface temperature, and a shift in wind direction are noted primarily between 1000 and 1300 UTC. *Smith et al.* [2010] provide a detailed analysis of SL4.

3.2.2.1. TRMM Microphysical Characteristics of SOP3 Squall Lines

[28] The TRMM microwave imager (TMI) provides inferred cloud properties such as liquid and ice cloud water, precipitation mass associated with falling hydrometers (rain and ice), and latent heat release. Figure 15 shows the precipitation mass for rain and ice for SL1, SL2, and SL3, where overpasses were available. SL1 on 19 August moved into dry air similar to SL4 on 11 September. This is reflected in the small precipitation mass found for liquid water (Figure 15a) for SL1 when compared to SL2 and SL3, where liquid water is found in amounts greater than 1 g/m^3 (Figures 15b and 15c). SL2 and SL3 lines had colder cloud tops and produced greater numbers of CG lightning flashes during their passage.

[29] A number of studies have shown that West African MCSs have large quantities of ice as determined by 85 GHz polarized corrected temperatures (PCT) [*Mohr and Zipser*, 1996] along with significant amounts of lightning. Figures 15d–15f show only modest amounts of ice mass above 6 km in SL1, but SL2 and SL3 show large ice mass in the upper troposphere. This is consistent with PCT values which are 170°K–190°K for SL1 but are less than 130°K for both SL2 and SL3 (not shown). Larger precipitation masses (ice and liquid) are also consistent with much larger latent heat release values in SL2 and SL3 (not shown).

3.3. SOP3 Phase III (16–30 September) and the FF-20 Aircraft Analysis

3.3.1. AEW and SAL Intrusions

[30] Figures 16a–16f show NCEP reanalysis and radiosonde data from Dakar, Senegal, for 16–30 September 2006. Meridional winds show approximately three AEW on 16, 19, and 26 September with the AEW on 19 September being associated with Hurricane Isaac (Figure 16b). There is some evidence of an AEW on 23 September (perturbation C) in the lower troposphere, which was sampled by the FA20 and discussed below. Strong zonal winds are found at midlevels during the period of 17 and 27–30 September in the NCEP reanalysis. The sounding data from Dakar shows a midlevel jet maximum on 19 September with a secondary low and midlevel wind maximum during the period of 27–30 September (Figure 16c). Dry air in the NCEP reanalysis is found during the time periods of 17, 21–23, and 27–30 September. This likely represents the retreat of the monsoon and end of the wet season as indicated by the lack of accumulated rain (Figure 1c), especially after Julian day 261 (18 September). Radiosounding data from Dakar show the highest relative humidity confined to the lower troposphere (>850 hPa) for most of the period except for 22 and 27–28 September (Figure 16e). Warm anomalies are found on 19, 22, and 27–30 September (Figure 16f).

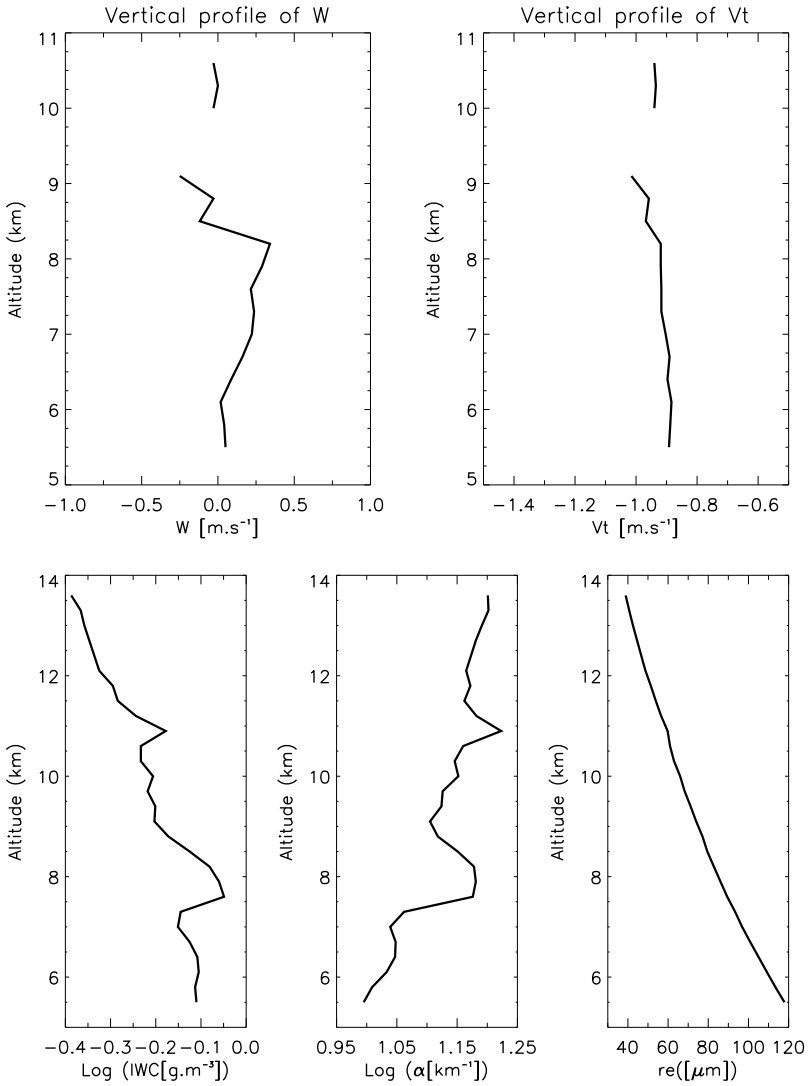

Figure 19. Mean vertical profile of (a) vertical air motion, (b) terminal fall velocity, (c) ice water content (IWC), (d) visible extinction, and (e) effective radius. These mean vertical profiles have been derived from all the Falcon 20 flights during AMMA SOP3.

3.3.2. FA/20 and 22 September Squall Line (SL5)

[31] On 22 September 2006, a fifth squall line (denoted as SL5), originating from the merging of less-organized small-scale convective cells in the early morning of 22 September 2006 at the Malian-Guinean border, reached the Kawsara region at approximately 1330 UTC (Figure 17a). The northern edge of SL5 is sampled by the NPOL radar during the afternoon. An active line of precipitation is observed at the leading edge of SL5 (Figure 17a) although the larger convective activity (based on MSG colder brightness temperature) is located farther south. This system propagates south-westward during the afternoon and rapidly dissipates rapidly as it reaches the ocean. This system was of particular interest for CloudSat validation since an A-Train overpass occurred at 1430 UTC (Figure 17e). This event was the purpose of a Falcon 20 flight (between 1415 and 1630 UTC) with a very good (spatial and temporal) colocation of the measurements along the spaceborne track. Simultaneous sampling in this deep precipitation system highlights the occurrence of multiple scattering in the spaceborne radar beam in the presence of strong attenuation [*Bouniol et al.*, 2008]. The amount of multiple scattering contamination is estimated as large as 4 dB (±2 dB) in this particular case and needs therefore to be corrected if quantitative use of the CloudSat radar reflectivity is to be made in these strong convective systems (ongoing work). The comparison of Figures 17d and 17e show that the RASTA measurements during the AMMA campaign lacks sensitivity, which limits its use for the characterization of the thinnest West African anvils.

[32] In addition to the CloudSat overpass, the cross-track organization of the convective system is also sampled by RASTA (Figure 17d). In addition to A-Train product evaluation, another objective of the Falcon-20 missions is to obtain a characterization of the microphysical and radiative properties as the convective systems moved into a coastal

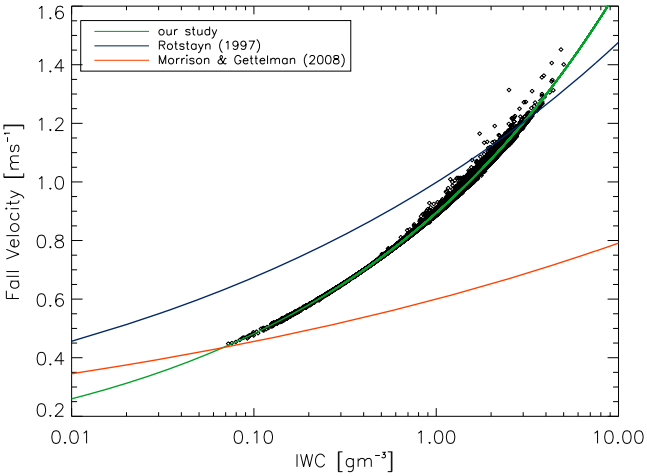

Figure 20. The statistical relationship between terminal fall velocity of ice crystals and ice water content derived from all Falcon 20 flights (blue data points, and red line for the fit to the data points) and from two GCM parameterization of the same statistical relationship: the *Rotstayn* [1997] parameterization of precipitating and cloud ice and the *Morrison and Gettelman* [2008] parameterization of precipitating ice.

environment. By making use of simultaneous radar and in situ probes measurements onboard the Falcon 20 aircraft, *Bouniol et al.* [2009] retrieved mean properties in the various regions of this particular MCS. For each particular region, a "most representative" density-diameter relationship (expressed as a power law relationship between ice hydrometeor density and maximum diameter) was proposed. This case is sampled at a nearly constant altitude (about 8 km altitude), but a rather large variability in the retrieved density-diameter relationship is found with denser hydrometeors in the thicker regions sampled (close to graupel density of *Locatelli and Hobbs* [1974]) and less dense hydrometers at the edges (southernmost and easternmost regions presenting lower reflectivity values in the Figure 17d), as expected. The variability of the particle size distribution has also been studied in the work of *Bouniol et al.* [2009]. For this particular case, it is found that in the central portions of convective systems, the particle size distribution is well approximated by an exponential function, while a larger slope is observed for the edges of the convective system.

[33] The RASTA observations collected during AMMA SOP3 are considered as a whole in order to characterize the statistical microphysical and radiative properties of the stratiform anvils generated by the deep convective activity in the Senegal region (land and ocean). One objective is to determine the potential variability of these properties over land and ocean. Therefore, from five Doppler measurements of the RASTA radar, the vertical wind component w is first separated from the terminal fall velocity of the ice hydrometeors V_F. Vertical profiles of the sum of these two contributions have been retrieved using a variational technique similar to that described in the work of *Protat and Zawadzki* [1999], but adapted to the geometry of RASTA observations. Then the so-called V_F-Z approach [*Protat et al.*, 2003; *Delanoë et al.*, 2007] is used to separate the two contributions. For all microphysical flights, the RASTA radar reflectivity and temperature profiles are used to retrieve the ice water content IWC (using the relationship recently proposed by *Matrosov and Heymsfield* [2008] for the ice part of convective systems), and the visible extinction α (using the *Heymsfield et al.* [2005] relationship), from which the effective radius, which is proportional to the ratio of IWC to α, is obtained.

[34] A highlight of the main results is provided in Figures 18, 19, and 20. First, a single V_F-Z relationship is developed using all the Dakar flights (Figure 18). From Figure 18, which displays the sum ($V_F + w$) as a function of 95 GHz radar reflectivity, a large (expected) spread around the fitted curve is obtained. In the V_F-Z approach, this spread is attributed to the contribution from the vertical wind speed [*Protat et al.*, 2003], which therefore indicates that vertical wind speeds are roughly within the range ± 2 m s^{-1} to in West African stratiform anvils. As also shown by the fitted curve in Figure 18, the terminal fall velocities range from 0.4 m s^{-1} for the smallest reflectivities (and therefore the smaller ice particles, presumably pristine ice crystals) to 1.7 m s^{-1} for the largest radar reflectivities (presumably corresponding to the ice aggregates formed when particles fall within the anvil and start aggregating with others in a warmer environment). These values are expected for ice hydrometeors [*Mitchell*, 1996].

[35] The statistical, dynamical, and microphysical properties of the anvils sampled during AMMA SOP3 over Dakar are also derived from a composite of all the Falcon 20 flights. A highlight of these statistical properties of West African anvils is given in Figure 19 as a mean vertical profile of terminal fall velocity, vertical wind component, ice water content, visible extinction, and effective radius. From Figure 19, several interesting features appear. First in terms of mesoscale dynamics (Figure 19a), the RASTA observations do confirm the earlier findings from GATE and COPT-81 that the ice part of stratiform anvils is generally characterized by a slow ascending vertical motion [*Chong et al.*, 1987], with an order of magnitude of 10–20 cm s^{-1}, peaking at 8–8.5 km altitude. This is in good agreement with the anvil observations from GATE and COPT-81 [*Chong et al.*, 1987; *Gamache and Houze*, 1982]. However, we find that mesoscale downward motions dominate in average above 8.5 km altitude, with peak values of about -40 cm s^{-1}, which is an unexpected feature not documented in earlier studies. This feature clearly requires further investigations.

[36] The vertical profile of terminal fall velocity is characterized by a very small trend with height, with values of about -0.9 m s^{-1}. However, the air density decreases exponentially with height; therefore, this constant vertical profile can be interpreted as much smaller particles at higher heights than at lower heights, which is expected in stratiform anvils due to aggregation processes. These suggestions are consistent with the respective vertical shapes of the IWC (Figure 19c), visible extinction (Figure 19d), and effective radius (Figure 19e) profiles. The largest vertical variation observed is for the effective radius, with mean values increasing from 40 mm at 13 km to 110 mm at 6 km, just above the melting layer (around 5 km), indicating that aggregation is a dominant mechanism. Consistent with this result is the slight increase in visible extinction, which is very sensitive to the particle concentration. This vertical variation of the effective radius and extinction is in very

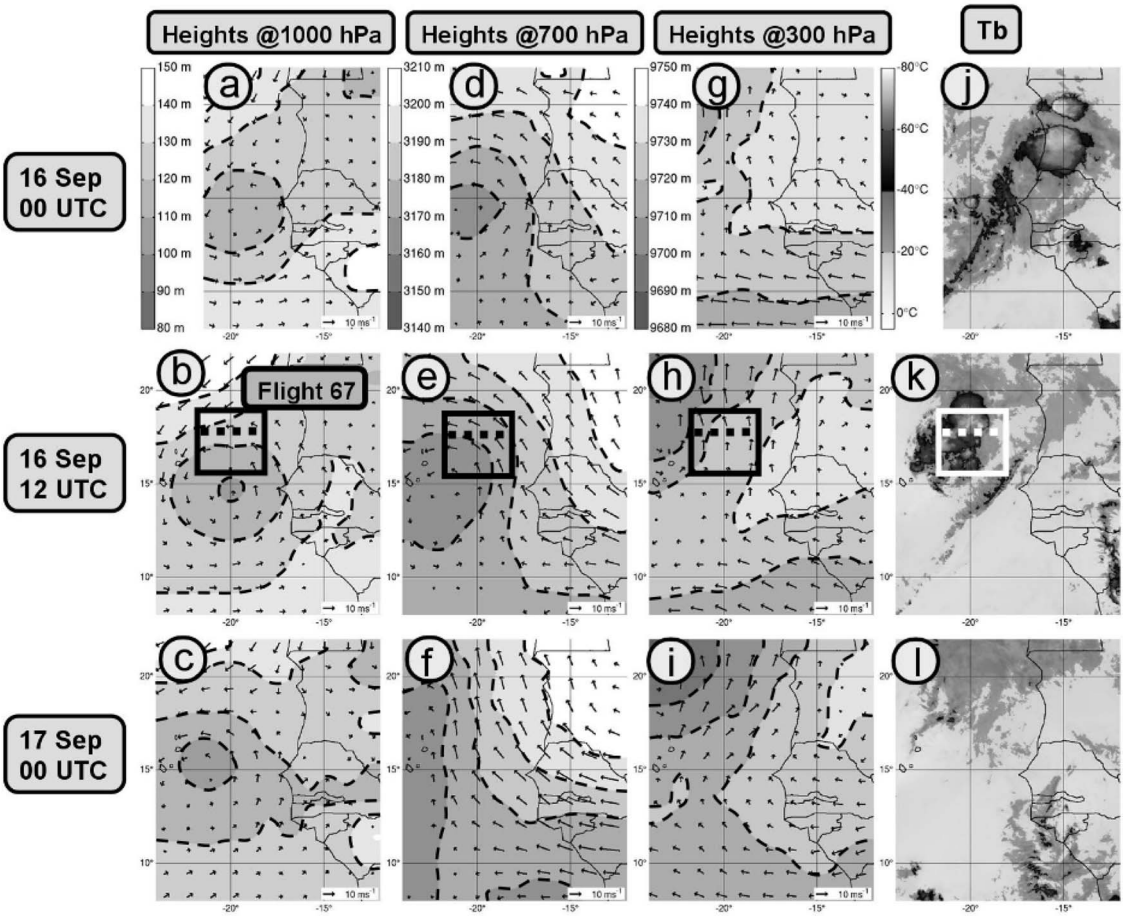

Figure 21. (a–c) Horizontal cross sections of geopotential height (m) and horizontal wind at 1000 hPa analyzed by ECMWF. (d–f) As in Figures 21a–21c, except at 700 hPa. (g–i) As in Figures 21a–21c, except at 300 hPa. (j–l) Brightness temperature (°C) in the water vapor channel at 7.3 μm from Meteosat-9. These images are from 16 September 2006 at 00 UTC (top: a, d, g, and j) until 17 September 2006 at 00 UTC (bottom: c, f, I, and l) with a time interval of 12 h. Heights and brightness temperature scales are indicated on the top left of each column. During flight 67 on 16 September 2006, eight successful dropsondes were launched between 1452 and 1642 UTC within an area delimited by the black squares in (b, e, h, and k). The dashed lines indicate the location of the zonal cross sections represented in Figure 22.

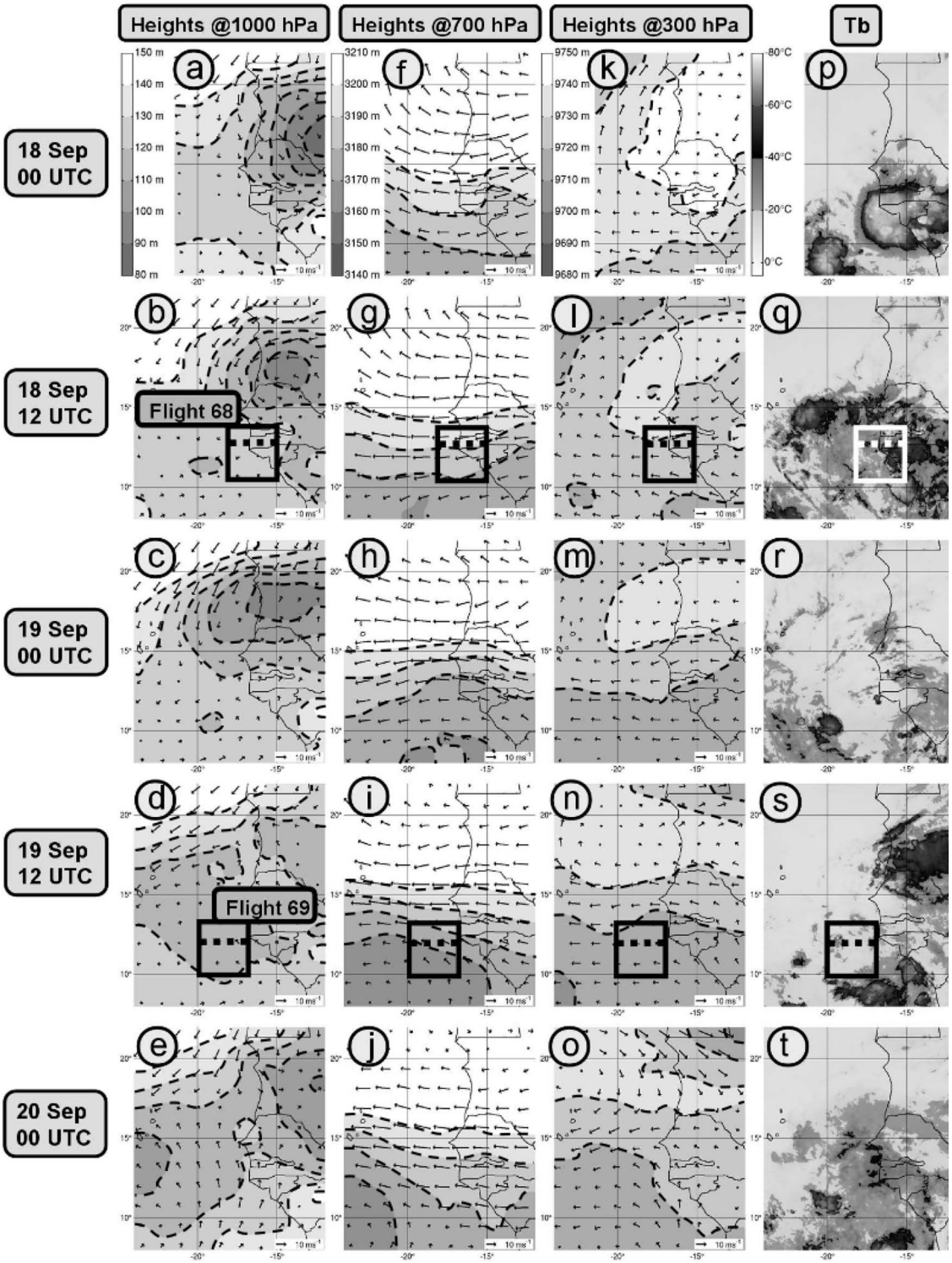

Figure 22. (a) Zonal cross section of relative vorticity (s^{-1}) obtained with dropsonde data of flight 67 in AMMA SOP3 (the location of these zonal cross sections is indicated by the dashed lines in Figure 21). The horizontal axis indicates longitude in degrees, and the vertical axis gives the altitude in meters. (b) As in Figure 22a, except for relative humidity (%). The gray-shaded scale of relative vorticity (relative humidity) is indicated on the top (bottom) right. The horizontal velocity is represented by arrows with the scale indicated in the bottom right.

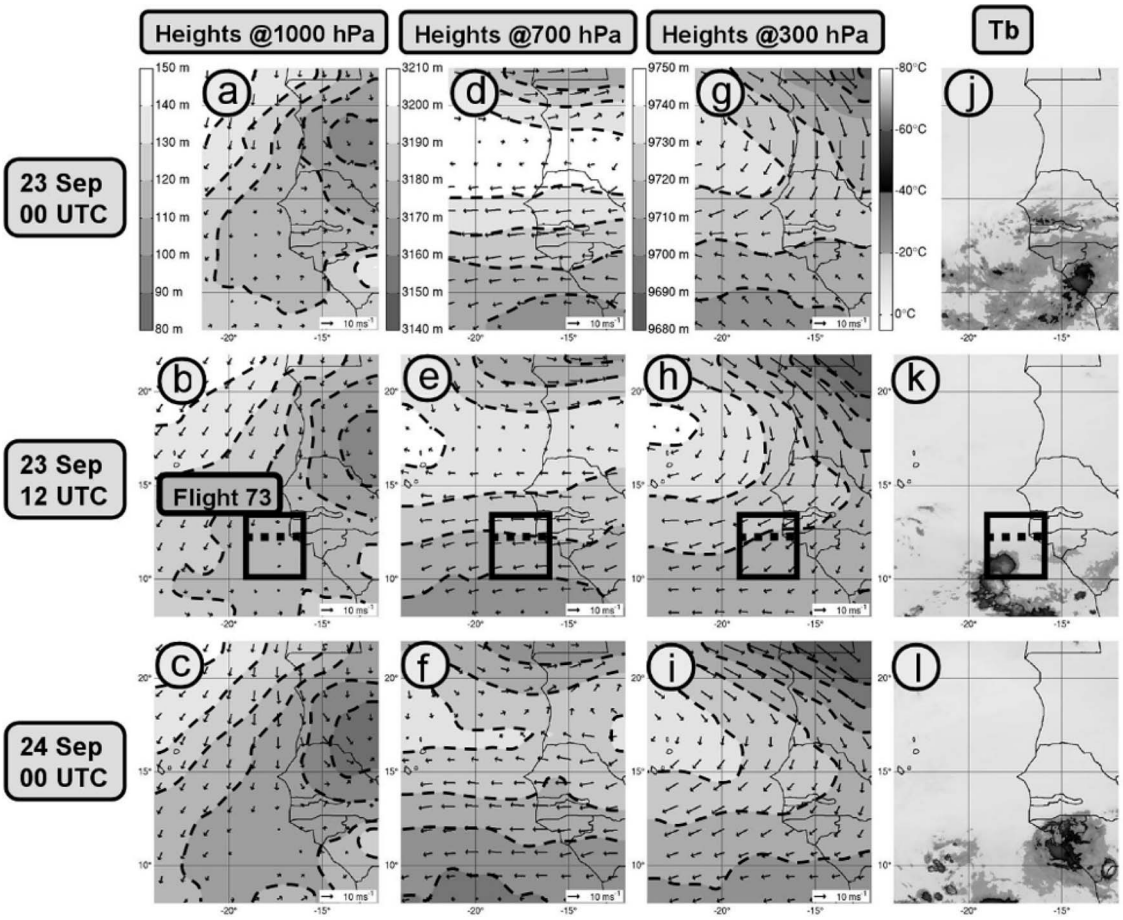

Figure 23. As in Figure 21, except from 18 September 2006 at 00 UTC (top: a, d, g, and j) until 20 September 2006 at 00 UTC (bottom: e, j, o, and t). During flight 68 on 18 September 2006, 10 successful dropsondes were launched between 1444 and 1646 UTC within an area delimited by the black squares in (b, g, l, q). The dashed lines indicate the location of the zonal cross sections represented in Figures 24a and 24b. During flight 69 on 19 September 2006, 12 successful dropsondes were launched between 1111 and 1312 UTC within an area delimited by the black squares in Figures 23d, 23i, 23n, and 23s. The dashed lines indicate the location of the zonal cross sections represented in Figures 22c and 22d.

good agreement with that found using ground-based radar-lidar observations over Niamey, Niger, and Darwin, Australia [*Protat et al.*, 2009], although the absolute values are much larger, which is expected since the data set used in the work of *Protat et al.* [2009] primarily consists of nonprecipitating anvils and cirrus clouds generated by the deep convective activity. However, aggregation of ice particles is not the only microphysical process active because ice water content was also observed to increase with temperature (or decreasing with height), probably reflecting the growth of ice crystals by water vapor deposition as the ice crystals fall within the anvil.

[37] This statistical characterization of the microphysical and radiative properties of stratiform anvils offers the unique opportunity to derive statistical relationships between these bulk microphysical properties specifically tailored for West African squall line anvils. These statistical relationships can be used either as a validation tool for different types of models or as direct statistical parameterizations in these models. For instance, a model in which ice water content is held as a prognostic variable could use the V_F-IWC relationship proposed in the present work to diagnose at each time step the ice hydrometeor fall speed. Among the different statistical relationships, this V_F-IWC relationship has been extensively studied with observations in order to provide observational constraints to ice cloud and precipitating ice fall speeds in global circulation models [*Heymsfield and Donner*, 1990; *Rotstayn*, 1997; *Morrison and Gettelman*, 2008]. As highlighted recently in the work of *Sanderson et al.* [2008], this fall speed parameter is one of the two producing most uncertainties in climate projections, and as discussed in the work of *Deng and Mace* [2008], the fall speed parameterization as a function of ice water content appears to be still very different amongst different models. Such a statistical relationship derived from our cloud radar observations of West African stratiform regions of squall lines is given in Figure 20. A nonlinear regression provides the following relationship:

$$V_F = 0.894\,\mathrm{IWC}^{0.269},$$

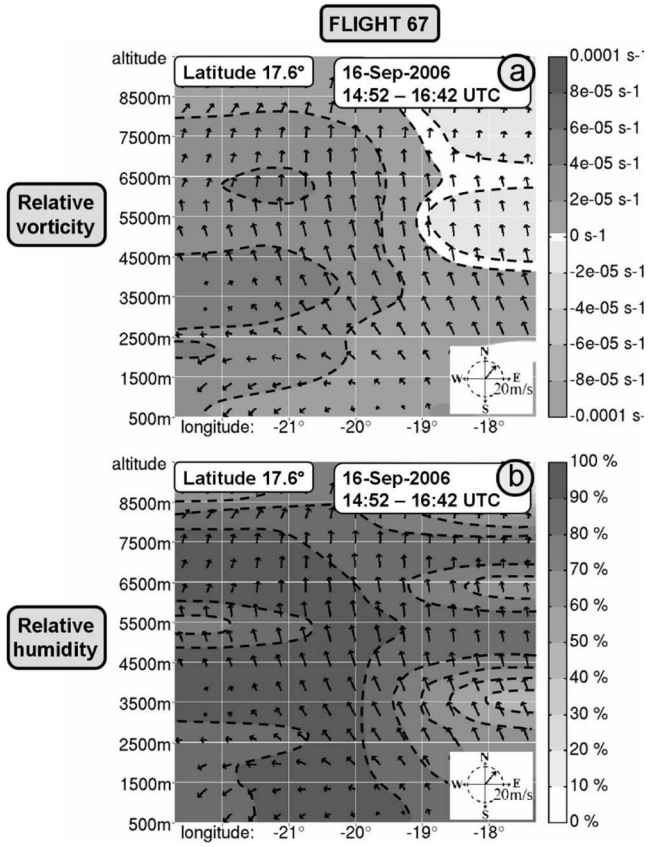

Figure 24. (a) As in Figure 22a, except for flight 69. (b) As in Figure 22a, except for flight 68. (c) As in Figure 22b, except for flight 68. (d) As in Figure 22b, except for flight 69. The locations of these zonal cross sections are indicated by the dashed lines in Figure 23.

with V_F in m s^{-1} and IWC in g m^{-3}. For the sake of comparisons, two widely used fall speed parameterizations from *Rotstayn* [1997] and *Morrison and Gettelman* [2008] are also displayed. From Figure 20, it appears clearly that the parameterization derived from our observations produce fall speeds, which agree fairly well with the formulation of *Rotstayn* [1997] for the largest IWCs but not for IWCs smaller than 0.3 g m^{-3}. In contrast, the *Morrison and Gettelman* [2008] parameterization agrees reasonably well with the fall speeds corresponding to these IWCs smaller than 0.3 g m^{-3} but produces significant underestimations of fall speeds associated with the largest IWCs, which was discussed in the work of *Sanderson et al.* [2008] probably has a very large impact on climate projections derived from the GCMs using this parameterization. This large underestimation of fall speeds associated with large IWC values is fairly consistent with the findings of *Deng and Mace* [2008], who showed that this *Morrison and Gettelman* [2008] fall speed parameterization was in fact more appropriate for cirrus clouds, since it agrees closely with the latest parameterization of cirrus fall speeds from *Deng and Mace* [2008].

3.3.3. Dropsonde Measurements of Perturbations A, B, and C During SOP3

3.3.3.1. Perturbation A

[38] On the morning of 16 September, perturbation A was associated with a closed cyclonic circulation in the low to midlevels and deep convection off the West African coast (Figure 21). However, during the afternoon, a midlatitude trough was approaching the region of Cape Verde Islands from northwest (Figure 21h and 21i), while the midlevel anticyclonic circulation of the AEW ridge east of perturbation A was increasing (Figures 21e and 21f). The increased southeasterly flow east of perturbation A sheared its midlevel cyclonic circulation. The convective activity dissipated while moving northward on 16 September evening and perturbation A failed to further develop.

[39] A composite vertical cross section from dropsonde data on 16 September (Figure 22) confirms that perturbation A was associated with cyclonic vorticity (up to $+6 \times 10^{-5}$ s^{-1}) and relatively moist air (relative humidity >90%) from the surface up to 9 km, west of 19°W. Figure 22 also reveals the adverse influence of relatively dry (relative humidity < 70%) and anticyclonic (up to -2×10^{-5} s^{-1}) air at midlevel from the west. This observation suggests the intensification of the AEW ridge east of perturbation A is related to dry anticyclonic Saharan air, probably in relation with the dynamics of the Saharan heat low. This dry air could also explain the weakening convective activity during the afternoon of 16 September (Figure 21l). The southerly flow in the mid and upper levels, which sheared the cyclonic circulation of perturbation A, is also visible in Figure 22.

3.3.3.2. Perturbation B

[40] Perturbation B was associated with a low-level closed vortex which crossed the Mauritanian coast (between 15°N and 20°N) on 18 September afternoon, a weak midlevel cyclonic circulation farther south (10°N–15°N), and weak convective activity off the West African coast (Figure 23). The low and midlevel cyclonic circulations merged during the night of 19–20 September, in association with disorganized convection. A remarkable characteristic of perturbation B is that it remained weakly active while moving westward, until it developed after the passage of a midlatitude trough and spawned Hurricane Isaac on 27 September near (26°N, 53°W).

[41] Composite vertical cross sections from the dropsonde data of 18 and 19 September show a substantial moistening of the atmosphere between the surface and 6 km, with relative humidity increasing from 60% to 80% (Figure 24). On 18 September, the system is associated with cyclonic vorticity (up to $+4 \times 10^{-5}$ s^{-1}) between 3 and 8 km and anticyclonic vorticity (up to -8×10^{-5} s^{-1}) below 3 km, as the dropsonde sampling is done south of the northern low-level vortex (Figure 23). This is a typical signature of an AEW trough with maximum intensity at midlevel. On 19 September, low-level vorticity is less anticyclonic (up to -2×10^{-5} s^{-1}), which corresponds to a more favorable environment for cyclogenesis. However, the lack of convective development prohibited any further evolution.

3.3.3.3. Perturbation C

[42] On 23 and 24 September, perturbation C is located off the West African coast and associated with a weak low to midlevel cyclonic circulation, anticyclonic conditions in the upper levels and weak convective activity (Figure 25). This system failed to further develop. A composite vertical cross section from the dropsonde data shows that perturbation C is embedded in a relatively dry (relative humidity < 80%) and weakly anticyclonic (up to -2×10^{-5} s^{-1}) air on 23 September between 1 and 4 km (Figure 26). The presence

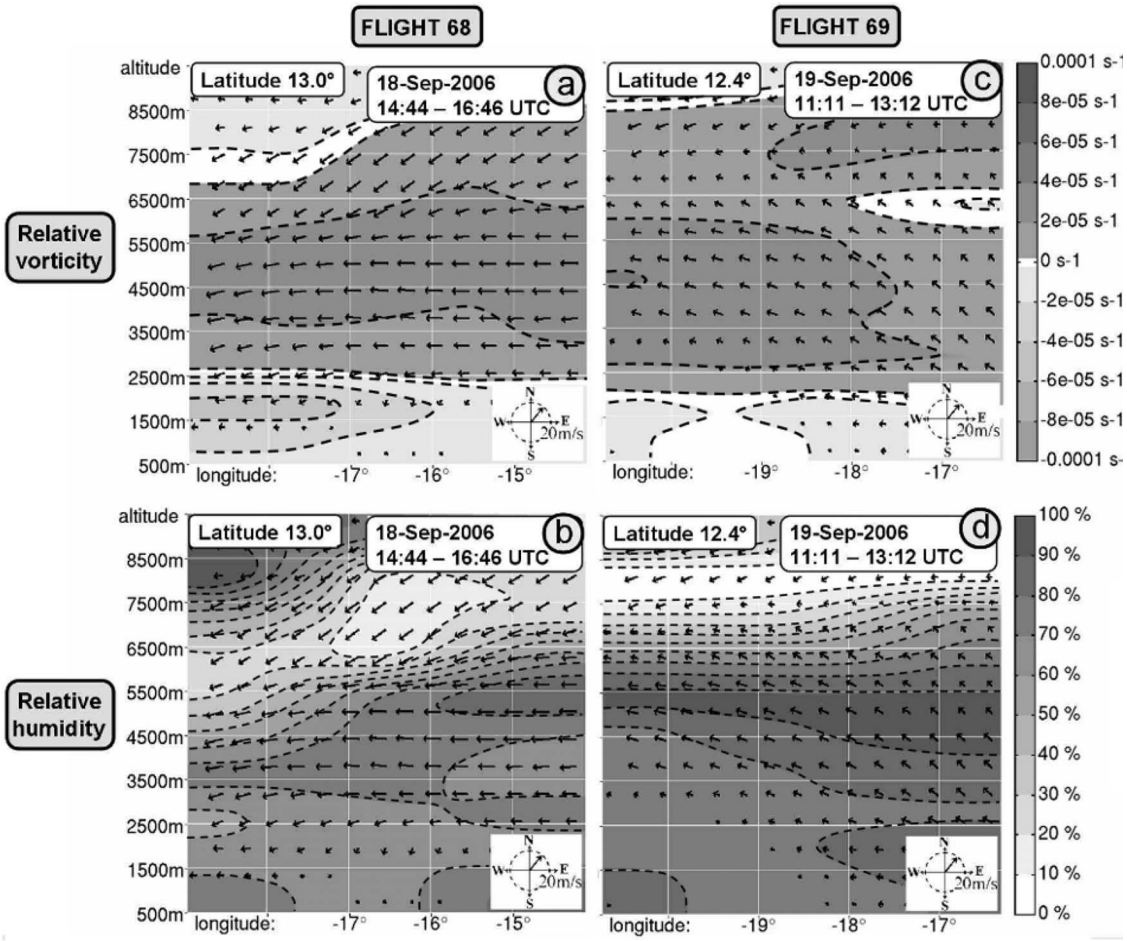

Figure 25. As in Figure 21, except from 23 September 2006 at 00 UTC (top: a, d, g, and j) until 24 September 2006 at 00 UTC (bottom: c, f, I, and l). During flight 73 on 23 September 2006, nine successful dropsondes were launched between 1118 and 1318 UTC within an area delimited by the black squares in Figures 25b, 25e, 25h, and 25k. The dashed lines indicate the location of the zonal cross sections represented in Figure 26.

of this dry air in the low levels certainly limited the convective activity observed by Meteosat-9 at that time. The flow is however weakly cyclonic between 4 and 9 km (up to 2×10^{-5} s^{-1}), as the dropsonde sampling was done south enough not to be influenced by the northern upper-level anticyclonic flow.

4. Summary and Conclusion

[43] During the period of 15 August and 30 September 2006, ground-based and aircraft measurements were conducted in a coastal environment (Senegal) during the AMMA SOP3 observing period. The measurements collected help in developing a better understanding of how AEWs and MCSs transition from a continental to marine environment. During this period, observations show as follows:

[44] 1. ten AEWs passing over or just south of Senegal with approximately 3 occurring per 15 days;

[45] 2. six SAL intrusions into Senegal; and

[46] 3. five squall lines (SLs).

[47] The passage of AEW through Senegal on 20 August and 2, 11, and, 19 September were associated with downstream developing tropical cyclones. SOP3 observations associated with the passage of the coastal SLs are consistent with earlier observations of SLs [*Houze*, 1977; *Chong et al.*, 1987; *Roux*, 1988] showing a reduction in air temperatures, shifts in wind direction, and an increase in surface pressure. All observed SLs were associated with CG lightning flashes with SL3 on 2 September showing the largest numbers of CG flashes. SL2 on 31 August showed the deepest convective core (reaching nearly 15 km) and was associated with CG lightning strikes. TRMM measurements show that SL2 and SL3 were associated with a significant ice amounts in the upper parts of the system while SL1 (19 August), SL4 (11 September), and SL5 (22 September) moved into a dry environment after a SAL outbreak and were weaker.

[48] FA20 aircraft measurements included Calipso/Cloudsat validation and provided a direct measurement of microphysical and mesoscale dynamics of mesoscale systems during 16–30 September. Measurements show weak mesoscale ascent below 8.5 km in the stratiform regions and

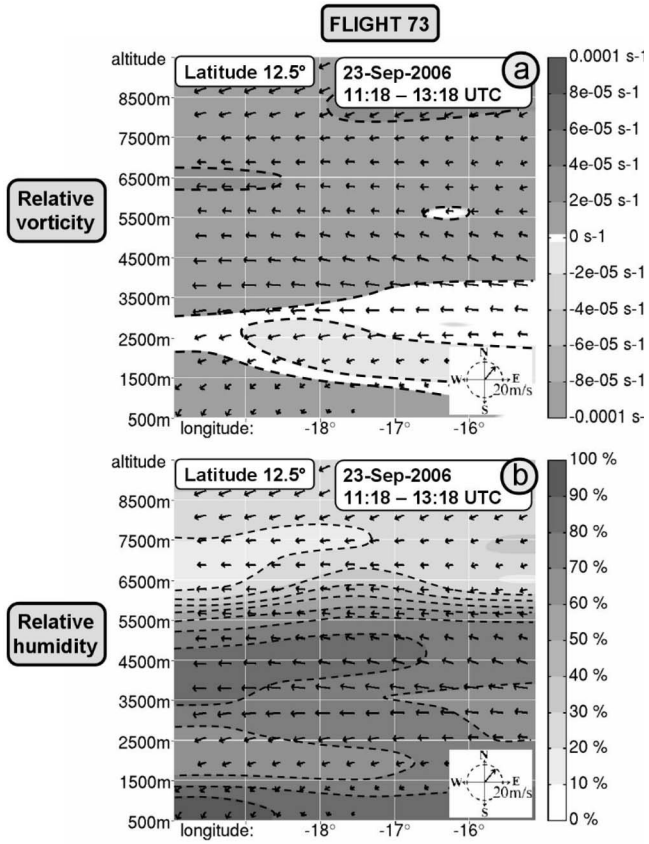

Figure 26. (a) As in Figure 22a, except for flight 73. (b) As in Figure 22b, except for flight 73. The location of these zonal cross sections is indicated by the dashed lines in Figure 25.

mesoscale descent above 8.5 km. Terminal fall velocities of hydrometers along with an empirical expression as a function of ice water content are derived based on FA20 measurements. Dropsondes from the FA20 confirm cyclonic vorticity at midlevels in perturbations A, B, and C and identified the role of upper-level features (troughs and ridges) in the nondevelopment of perturbation A. Upper-level circulations also played a role in the nondevelopment case of perturbation D (Arnault and Roux, submitted manuscript).

[49] This field campaign is the first large-scale experiment in coastal zones since the GATE field campaign of 1974 and comes after a significant period of below normal rainfall in West Africa [*Nicholson et al.*, 2000]. Long-term measurements are required for understanding the interactions between the SAL, AEWs, MCSs (particularly squall lines), and their linkages to seasonal, annual, and decadal rainfall variability. The potential hazards from MCSs or strong convection associated with AEWs should be monitored for welfare of vulnerable populations in West Africa. Moreover, because a significant fraction of Atlantic hurricanes evolve from AEWs, which may threaten central American, Caribbean, or coastal U. S. communities, it is critical to maintain and increase West African observations that can be used to improve numerical weather model initialization. This field campaign also provided a unique opportunity for students in Senegal and the United States to help advance scientific knowledge [*Smith et al.*, 2009] and future opportunities should be encouraged [*Jenkins and Gaye*, 2010].

[50] **Acknowledgments.** We are thank U. S. and Senegalese students Nyasha George, Deanne Grant, Marcia DeLonge, Aaron Pratt, Stephen Chan, Daniel Robertson, Segayle Walford, Tamara Battle, Christopher Foltz, Aaron Pratt, Andrew Newmann, Samo Diatta, and Thioro Fall for their extraordinary efforts during SOP3. We also thank D. Tanre for use of the Mbour AERONET data. This work was funded by NASA grant NNX06AC78G.

References

Arnault, J., and F. Roux (2010), Failed cyclogenetic evolution of a West African monsoon perturbation observed during AMMA SOP-3, *J. Atmos. Sci.*, *67*, 1863–1883.

Bouniol, D., A. Protat, A. Plana-Fattori, M. Giraud, J.-P. Vinson, and N. Grand (2008), Comparison of airborne and spaceborne 95-GHz radar reflectivity and evaluation of multiple scattering effects in spaceborne Measurements, *J. Atmos. Oceanic Technol.*, *25*, 1983–1995, doi:10.1175/2008JTECHA1011.1.

Bouniol, D., J. Delanoë, C. Duroure, A. Protat, V. Giraud, and G. Penide (2009), The microphysical characterisation of West African mesoscale convective anvils, *Quart. J. Roy. Meteor. Soc.*, *136*(S1), 323–344, 2010, doi:10.1002/qj.557.

Burpee, R. W. (1975), Some features of synoptic-scale waves based on compositing analysis of GATE data, *Mon. Weather Rev.*, *103*, 921–925.

Chong, M. P., P. Amayenc, G. Scialom, and J Testud (1987), A tropical squall line observed during the COPT-81 experiment in West Africa: Part 1. Kinematic structure inferred from dual Doppler radar data, *Mon. Weather Rev.*, *115*, 670–694.

D'Amato, N., and T. Lebel (1998), On the characteristics of the rainfall events in the Sahel with a view to the analysis of climatic variability, *Int. J. Climatol.*, *18*, 955–974.

Delanoë, J., A. Protat, D. Bouniol, A. J. Heymsfield, A. Bansemer, and P. R. Brown (2007), The characterization of ice cloud properties from Doppler radar measurements, *J. Appl. Meteor.*, *46*, 1682–1698.

Delonge, M. S., et al. (2010), Attributes of mesoscale convective systems at the land-ocean transition in Senegal during NASA African Monsoon Multidisciplinary Analyses 2006. Attributes of mesoscale convective systems at the land-ocean transition in Senegal during NAMMA-06, *J. Geophys. Res.*, *115*, D10213, doi:10.1029/2009JD012518.

Deng, M., and G. G. Mace (2008), Cirrus cloud microphysical properties and air motion statistics using cloud radar Doppler moments: Water content, particle size, and sedimentation relationships, *Geophys. Res. Lett.*, *35*, L17808, doi:10.1029/2008GL035054.

Fortune, M. (1980), Properties of African squall lines inferred from time lapse satellite imagery, *Mon. Weather Rev.*, *108*, 153–168.

Gamache, J. F., and R. A. Houze (1982), Mesoscale Air Motions Associated with a Tropical Squall Line, *Mon. Wea. Rev.*, *110*, 118–135.

Gaye, A. T., A. Viltard, and P. de Felice (1995), Squall lines and rainfall over West Africa during summer 1986 and 87, *Meteor. and Atmos. Physics*, *90*, 215–224.

Grant, D. D., et al. (2008), Ozone transport by mesoscale convective systems in western Senegal, *Atmos. Environ.*, *42*, 7104–7114.

Gray, W. M., and C. Landsea (1992), African rainfall as a precursor of hurricane-related destruction on the U. S. east coast, *Bull. Am. Meteorol. Soc.*, *73*, 1352–1364.

Heymsfield, A. J., and L. J. Donner (1990), A scheme for parameterizing ice-cloud water content in general circulation models, *J. Atmos. Sci.*, *47*, 1865–1877.

Heymsfield, A. J., D. Winker, and G.-J. van Zadelhoff (2005), Extinction-ice water content-effective radius algorithms for CALIPSO, *Geophys. Res. Lett.*, *32*, L10807, doi:10.1029/2005GL022742.

Houze, R. A. (1977), Structure and dynamics of a tropical squall-line system, *Meteorol. Atmos. Phys.*, *105*, 1540–1567.

Jenkins, G. S., and A. T. Gaye (2010), Addressing relevant policy driven weather and climate topics through international field experiences in Senegal for underrepresented students in the United States and Senegal, *Bull. Am. Meteorol. Soc.*, in review.

Jenkins, G. S., A. Pratt, and A. Heymsfield (2008), Possible linkages between Saharan dust and tropical cyclone rain band invigoration in eastern Atlantic during NAMMA-06, *Geophys. Res. Lett.*, *35*, L08815, doi:10.1029/2008GL034072.

Kalnay, E., et al. (1996), The NCEP/NCAR 40 year reanalysis project, *Bull. Am. Meteorol. Soc.*, *77*, 437–471.

Keogh, S. J., E. Hibbett, J. Nash, and J. Eyre (2007), The Met office arrival time difference (ATD) system for thunderstorm detection and lightning location. Forecasting Research Technical Report 488.

Laing, A. G., J. M. Fritsch, and A. J. Negri (1999), Contribution of mesoscale convective complexes to rainfall in Sahelian Africa: Estimates from geostationary infrared and passive microwave data, *J. Appl. Meteorol.*, *38*, 957–964.

Landsea, C., and W. Gray (1992), The strong association between the Western Sahelian monsoon rainfall and intense Atlantic hurricanes, *J. Clim.*, *5*, 435–453.

Locatelli, J. D., and P. V. Hobbs (1974), Fall speeds and masses of solid precipitation particles, *J. Geophys. Res.*, *79*(15), 2185–2197, doi:10.1029/JC079I015P02185.

Mathon, V., and H. Laurent (2001), Life cycle of Sahelian mesoscale convective cloud systems, *Q. J. R. Meteorol. Soc.*, *127*, 377–406.

Matrosov, S. Y., and A. J. Heymsfield (2008), Estimating ice content and extinction in precipitating cloud systems from CloudSat radar measurements, *J. Geophys. Res.*, *113*, D00A05, doi:10.1029/2007JD009633.

Mitchell, D. L. (1996), Use of Mass- and Area-Dimensional Power Laws for Determining Precipitation Particle Terminal Velocities, *J. Atmos. Sci.*, *53*, 1710–1723.

Mohr, K. I., and E. J. Zipser (1996), Defining mesoscale convective systems by the 85-GHz ice scattering signatures, *Bull. Am. Meteorol. Soc.*, *77*, 1179–1188.

Moine, M.-P. (2001), Structure et evolution à mésoéchelle de perturbations cycloniques de l'Atlantique Nord pendant FASTEX, Thèse de l'Université Paul Sabatier, Toulouse III, France.

Morrison, H., and A. Gettelman (2008), A new two-moment bulk stratiform cloud microphysical scheme in the Community Atmosphere Model (CAM3): Part I. Description and numerical tests, *J. Clim.*, *21*, 3642–3659.

Nesbitt, S. W., E. J. Zipser, and D. J. Cecil (2000), A census of precipitation features in the tropics using TRMM: Radar, ice scattering, and lightning observations, *J. Clim.*, *13*, 4087–4106.

Nicholson, S. E., B. Some, and B. Kone (2000), An analysis of recent rainfall conditions in West Africa, including the rainy seasons of the 1997 El Niño and the 1998 La Niña years, *J. Clim.*, *13*, 2628–2640.

Protat, A., J. Delanoë, A. Plana-Fattori, P. T. May, and E. O'Connor (2009), The statistical properties of tropical ice clouds generated by the West-African and Australian monsoons from ground-based radar-lidar observations, *Quart. J. Roy. Meteor. Soc.*, *136*(S1), 345–363, 2010, doi:10.1002/qj.490.

Protat, A., and I. Zawadzki (1999), A variational method for real-time retrieval of three-dimensional wind field from multiple-doppler bistatic radar network data, *J. Atmos. Oceanic Technol.*, *16*(4), 432–449.

Protat, A., Y. Lemaître, and D. Bouniol (2003), Terminal fall velocity and the FASTEX cyclones, *Quart. J. Roy. Meteor. Soc*, *129*, 1513–1535.

Redelsperger, J.-L., et al. (2006), African monsoon multidisciplinary analysis: An international research project and field campaign, *Bull. Am. Meteorol. Soc.*, *87*, 1739–1746.

Rotstayn, L. D. (1997), A physically based scheme for the treatment of stratiform clouds and precipitation in large-scale models: I. Description and evaluation of the microphysical processes, *Q. J. R. Meteorol. Soc.*, *123*, 1227–1282.

Roux, F. (1988), The West African squall line observed on 23 June 1981 during COPT 81: Kinematics and thermodynamics of the convective region, *J. Atmos. Sci.*, *45*, 406–426.

Roux, F., J. Testud, M. Payen, and B. Pinty (1984), West African Squall-Line Thermodynamic Structure Retrieved from Dual-Doppler Radar Observations, *JAS*, *41*, 3104–3121.

Sall, S. M., and H. Sauvageot (2005) Cyclogenesis of the African coast: The case of Cindy in August 1999, *Meteorol. Atmos. Phys.*, *133*, 2803–2813.

Sanderson, B. M., C. Piani, W. J. Ingram, D. A. Stone, and M. R. Allen (2008), Toward constraining climate sensitivity by linear analysis of feedback patterns in thousands of perturbed-physics GCM simulations, *Clim. Dyn.*, *30*, 175–190.

Sealy, A, G. S. Jenkins and S. C. Walford (2003), Seasonal/regional comparisons of rain rates and rain characteristics in West Africa using TRMM observations, *J. Geophys. Res.*, *108*(D10), 4306, doi:10.1029/2002JD002667.

Smith, J. W., et al. (2010), Linkages between an 11 September 2006 West African Squall Line and Saharan Air Layer Outbreak during NAMMA-06, *submitted to Atmospheric Chemistry Physics*.

Stephens, G. L., et al. (2002), The CLOUDSAT mission and the A-train, *Bull. Am. Meteorol. Soc.*, *83*, 1771–1790.

Zipser, E. J., and C. Gautier (1978), Mesoscale events with a GATE tropical depression, *Meteorol. Atmos. Phys.*, *106*, 789–805.

Zipser, E. J., C. H. Twohy, S. C. Tsay, K. L. Thornhill, S. Tanelli, et al. (2009), The Saharan Air Layer and the Fate of African Easterly Waves NASA's AMMA 2006 Field Program to Study Tropical Cyclogenesis: NAMMA, *Bull. Amer. Meteor. Soc.*, *90*, 1137–1156.

J. Arnault and F. Roux, Laboratoire d'Aérologie, Observatoire Midi-Pyrénée, 14 av. Belin, F-31400 Toulouse, France.

D. Badiane, A. Deme, A. Gaye, F. Kebe, S. A. Ndiaye, and S. Sall, Laboratory for Atmospheric-Oceanic Simeon Fongang (LPAO-SF), Cheikh Anta Diop University, Dakar, Senegal.

D. Bouniol, GAME/CNRM, CNRS/Météo-France, Toulouse, France.

M. Camara, Department of Physics, University of Ziguinchor, Ziguinchor, Senegal.

J. Fuentes, Department of Meteorology, The Pennsylvania State University, University Park, PA 16802, USA.

J. Gerlach, NASA Wallops Flight Facility, Wallops, VA 23337, USA.

G. Jenkins and E. Joseph, Department of Physics and Astronomy, Howard University, Washington, DC 20059, USA. (gregory.s.jenkins@gmail.com)

P. Kucera, National Center for Atmospheric Research, Boulder, CO 80307, USA.

M. Papazzoni and N. Viltard, LATMOS (Laboratoire Atmosphères, Milieux, Observations Spatiales), Vélizy, France.

A. Protat, CAWCR (Centre for Australian Weather and Climate Research), Melbourne, Australia.

A. Reynolds, NASA Goddard Space Flight Center, Greenbelt, MD 20770-2548, USA.